EXPERIMENTAL INVESTIGATION OF SOLID AND LIQUID AEROSOL TRANSPORT IN A HORIZONTAL SQUARE CHANNEL

A Thesis

by

REYNALDO CHAVEZ JR.

Submitted to the Office of Graduate and Professional Studies of
Texas A&M University
in partial fulfillment of the requirements for the degree of

MASTER OF SCIENCE

Chair of Committee,	Nagamangala K. Anand
Committee Members,	Thien D. Nguyen
	Yassin A. Hassan
	Piyush Sabharwall
Head of Department,	Andreas A. Polycarpou

August 2020

Major Subject: Mechanical Engineering

ABSTRACT

Various industrial applications such as medical/pharmaceutical sprays, heating, ventilation and air conditioning systems, and other solid/liquid atomization processes benefit from the characterization of flow and deposition mechanisms of solid/liquid aerosols. This work aimed to experimentally study the transport of solid and liquid aerosol particles which represented aerosolized fission products in a nuclear reactor. We measured the flow field, free-stream concentration, and surface deposition of solid/liquid aerosols flowing in a horizontal square channel with Reynolds number of 750-$7,000$. Particle image velocimetry (PIV) was applied to acquire the flow field characteristics such as mean velocity fields and turbulent kinetic energy. The effects of Reynolds number and particle diameter were investigated by studying the particle deposition and penetration of two micron-sized particle types. The experimental results of particle deposition velocity agreed well with the correlations published previously and with the associated numerical results. For the Reynolds numbers tested in this study, solid and liquid particle deposition was found to be governed by gravitational sedimentation. Increasing the Reynolds number for a given particle diameter increased the particle relaxation time and penetration efficiency but decreased the particle deposition velocity. Decreasing the particle diameter for a given Reynolds number increased the effect of gravitation sedimentation. By altering the surface properties with the addition of a carbon nanotube coating, the penetration was shown to decrease for the same flow conditions when compared with a smooth surface. Secondary flow vortices located in the corners, unique to turbulent flow in a square channel, were experimentally shown to increase particle deposition in the corners.

DEDICATION

This thesis is dedicated to the Chavez family. Without the memories to fall back on, I am not sure I could have made it this far. To my brother and sister, we may have different paths in life but I am blessed to have started mine with you two. To my father, thank you for drilling in the desire for perfection and the satisfaction which comes with competition. To my mother, thank you for providing calm, caring words throughout the years and for showing me that patience with one's self allows you to maneuver through life rather than having life steer you.

Last but not least, I would like to dedicate this thesis to those who have inspired me. To Navin and Aditya, thank you for bringing me in, befriending me, and all the encouragement you have given me at this level. You two have taught me the graduate student's landscape, how to navigate through it, and how to be successful under the most demanding and time-consuming circumstances.

ACKNOWLEDGMENTS

I would like to acknowledge the combined efforts of graduate/undergraduate students at the Texas A&M University Thermal-Hydraulic Research Laboratory for helping me overcome obstacles with the experiment or analysis which led to the completion of this experimental study. Special thanks to Professor N.K. Anand, Professor Thien Nguyen, and Professor Yassin Hassan for the guidance, patience, and opportunity. I would also like to acknowledge Daniel Orea, Blake Maher, Robert Muyshondt, Vanessa Gutierrez, Nathan Mitchell, and Luma Al-Mahbobi.

CONTRIBUTORS AND FUNDING SOURCES

Contributors

This work was supported by a thesis committee consisting of Professor N.K. Anand (chair), Professor Thien D. Nguyen, Professor Yassin A. Hassan, and Dr. Piyush Sabharwall.

The PIV data taken at the middle of the test section was analyzed by Professor Thien D. Nguyen and Daniel Orea. The numerical simulation results depicted in Figure 7.9 were generated by Byung-Hee Choi. All other work conducted for the thesis was completed by the student independently.

Funding Sources

This work is partially funded by the U.S. Department of Energy Office of Nuclear Energy's Versatile Test Reactor program. Graduate study was supported by a graduate assistantship from Texas A&M University.

NOMENCLATURE

Abbreviations

APS	Aerodynamic Particle Sizer
CCD	Charged Couple Device
CNT	Carbon Nano-Tube
DEHS	Di-Ethyl-Hexyl-Sebacate
GFR	Gas-Cooled Fast Reactors
OPS	Optical Particle Sizer
PIV	Particle Image Velocimetry
SAG	Solid Aerosol Generator
SPI	Solid Particle Injector
TKE	Turbulent Kinetic Energy
VTR	Versatile Test Reactor

Symbols and Greek Letters

α	Image magnification factor (mm/pixel)
$\dot{m}_{SPI}$	Injection rate of the SPI (g/s)
μ_f	Dynamic viscosity of fluid (Pa·s)
ν_f	Kinematic viscosity of fluid (m^2/s)
$\rho_{f,part}$	Density of fluid or particle (kg/m^3)

τ^+_{part}	Non-dimensional particle relaxation time
τ_w	Wall shear stress (Pa)
$A_{img,part}$	Image area or particle cross sectional area (m^2)
$c_{in,out}$	Free stream particle concentration at inlet/outlet of test section ($\#/m^3$)
D_p	Particle mass diffusivity (m^2/s)
f	Friction factor
g^+	Non-dimensional acceleration due to gravity
$J_{avg,i}$	Particle flux to the wall ($\#/m^2 \cdot s$)
k	Boltzmann's constant (J/K)
$N_{dep,in,out}$	Number of particles deposited, injected, or leaving the test section ($\#$)
$R_{uu,vv}$	$= \bar{u'}^2, \bar{v'}^2$ Reynolds normal stress for the u and v components
Re	Reynolds Number
Sc	Schmidt Number
Stk	Particle Stokes Number
$t_{injection}$	Time after particle injection (s)
u', v'	Fluctuating u, v velocity (m/s)
u^*	Friction velocity (m/s)
u^+	Normalized u velocity
u^+_d	Non-dimensional particle deposition velocity
u^+_{RMS}	RMS of normalized fluctuating u velocity

u_{rel}	Relative velocity of the particle to the fluid (m/s)
V_{part}	Volume of particle (m^3)
y^+	Non-dimensional wall distance
d	Diameter (m)
g	Gravitational constant (m/s^2)
L	Characteristic length
P	Penetration efficiency
T	Absolute temperature (K)
x-,y-,z-	Horizontal (Stream-wise), vertical, lateral directions

Subscripts

avg	average
CNT	CNT-coated surface condition
d,dep	deposition
f	fluid (air)
h	hydraulic
img	image
i	instantaneous
$liquid$	liquid particle
m	model
$part$	particle

$_p$	prototype
$_{RMS}$	Root Mean Square
$_{smooth}$	smooth surface condition
$_{solid}$	solid particle
$_w$	wall

TABLE OF CONTENTS

Page

LIST OF FIGURES

FIGURE Page

LIST OF TABLES

TABLE Page

1. INTRODUCTION AND LITERATURE REVIEW

1.1 Background

Numerous applications are affected by particle transport and deposition, such as fabrication of microelectronics, ventilation systems for residential buildings, and human airway inhalation. Therefore, multiple studies have focused on particle deposition. For instance, research has been conducted on particle deposition in airway bifurcation to understand the effects of particulate matter in the human respiratory system (Tsuda et al., 2011; Zhang et al., 2002; Asgharian and Anjilvel, 1994). In addition, the deposition and suspension behaviors of large particles (Aluko and Noll, 2006) and particles with uncommon shapes (Kvasnak and Ahmadi, 1995) have been studied to expand the understanding of particle deposition in channel flow. In particular, another application of particle transport behavior is in the safety assessment of nuclear gas-cooled reactors. Fischer et al. (2018) used graphite particles and helium to simulate a contaminated reactor coolant emerging from relative motion between fuel elements or from contact with the graphitic reflector structure. Similarly, this study explores particle deposition mechanisms in channel flow that have potential applications in gas-cooled reactors.

In gas-cooled fast reactors (GFR), fission products such as particulate matter and gases may be released into the primary system and/or into the reactor containment building, making these fission products a potential source of particulate matter. Such particulate matter can range in size from the sub-micron level to an order of 10μm (Humrickhouse, 2011). The measurement techniques developed in this work to investigate the transport of particulate matter will be ultimately tested in a scaled GFR experimental facility. Prior to applying the measurement techniques to the GFR experimental facility, it is important to verify and validate the techniques and the uncertainties associated with them. This is accomplished by conducting experimental measurements in a horizontal square channel.

1.2 Objective

In this work, the objective was to develop advanced techniques to characterize transport of surrogate fission products (particles) in prototypical environments. This work is also meant to support the quantification of fission product release, transport, deposition, and resuspension. Likewise, the data obtained in this work is a means to provide supporting data for developing numerical models and system codes for the Versatile Test Reactor (VTR) program where the phenomena connected to the transport, deposition, and possible resuspension are important to the reactor safety.

1.3 Literature Review

A review on the published literature on particle deposition in rectangular and circular channels is provided in Table 1.1. While reviewing previously reported studies, the following gaps were noted. To the best of this author's knowledge, flow passages in GFRs carrying particles and fission products are mostly rectangular or circular channels. Moreover, the majority of studies on particle deposition in square channels are limited. In Table 1.1, a summary of the experimental techniques implemented to measure concentration, flow fields, and/or surface deposition is provided. These studies used air as the fluid and various particle types. The authors primarily utilized a mass difference technique to quantify surface deposition. By quantifying mass difference, the surface deposition of solid phase particles can be reasonably estimated, but only the cumulative surface deposition can be quantified. In contrast, an imaging technique offers both instantaneous and cumulative deposition information. Likewise, no experimental work was found on the local stream-wise surface deposition of particles along the length of the channel or local surface deposition of particles in the lateral direction to flow. The lack of literature on the lateral distribution of particle deposition in rectangular/square channels has been noted because numerical studies (Galletti and Bottart, 2004; Sharma and Phares, 2006; Phares and Sharma, 2006; Choi et al., 2019) have shown increased particle deposition in the corners caused by secondary flow vortices. In this study, particles were used to represent accident scenarios of leakage of solid/liquid particulate matter in a GFR facility. Therefore, it is important to capture these particles from flow in a depressurization

scenario and to explore filtration methods that enhance deposition. Thus, numerous studies have explored particulate filtration through a carbon nanotube (CNT) sheets; however, no experimental studies were found on the effect of adding a CNT surface coating on particle deposition to channel walls. Likewise, only few studies (Wells and Chamberlain, 1967; Gutfinger and Friedlander, 1985) have measured and discussed the impact of fibrous elements protruding from the surface on the enhancement of deposition. The present study was performed to address the above identified gaps.

In this study, surrogate particle deposition was analyzed in a horizontal square channel using air as the working fluid and polypropylene microspheres and (DEHS) droplets as surrogate particles. Surrogate particles were considered to study the aerodynamic behavior of fission particles based on the dynamic similarity through matching Stokes and Reynolds numbers. Depending on the Reynolds numbers of the flow and the Stokes numbers of the particle, the deposition of particulates released into the square channel is affected by mechanisms such as gravitational settling, Brownian diffusion, turbophoresis, and eddy-impaction (Liu and Illori, 1973). In the turbulent diffusion-eddy impaction regime, the particle drift mechanism known as turbophoresis becomes important. Originally described by Caporaloni et al. (1975) and Reeks (1983), turbophoresis describes the transmission of particles from an area of high turbulent mixing to an area with a lower degree of mixing. Particle suspended in a turbulent flow are dispersed randomly and the degree of dispersion is inherent to the degree of mixing. Therefore, with all other mechanisms held equal, turbophoresis explains how particles migrate to a lower turbulence region. The particles in this study had small Stokes number in order for the particle trajectories to follow the flow streamlines. In this regard, inertial forces played a small role in deposition. Likewise, Brownian motion played a very small role since the size of the particles in this study was large enough as to not have their trajectories altered by collisions with the random motion of gas molecules. Lastly, the particles studied here had a relaxation time of $\tau^+ \leq 1$ and for relaxation times of this order, the resulting deposition is ultimately caused by gravitational sedimentation and turbulent diffusion.

The particle relaxation times considered in this work were primarily in the gravitational sedi-

mentation regime for both the polypropylene microsphere particles and the DEHS droplets. Under this regime, particle deposition is driven by the influence of a gravity induced drag force on particle migration to the wall as well as turbulent air eddies that direct the motion of the particles which occur in response to sporadic, violent eruptions of the viscous sublayer, as observed by Kline et al. (1967). Owen (1969) first proposed that particles are convected to the wall and that deposition to the wall could be described using an equation of the form $u_d^+ = \mathbf{K}\tau^{+2}$, where $\mathbf{K}$ is a constant. Later, Wood (1981b) showed that Owen's model accurately described the deposition velocity in the eddy diffusion-impaction regime but failed in the turbulent diffusion regime. This work adopted Wood's model for comparison with calculated particle deposition velocities. The adopted model included terms which numerically described the effects of Brownian diffusion, eddy diffusion-impaction, and gravitational sedimentation (Kvasnak et al., 1993).

In this study, we developed experimental techniques to measure the flow field, free-stream particle concentration, and surface deposition and applied the methods to quantify the mean velocity vector field, dimensionless deposition velocity, penetration efficiency, and stream-wise/lateral deposition distribution. The flow field in a square channel was measured using particle-image velocimetry (PIV). The particle concentrations inside the channel and on the bottom wall were measured using an optical particle sizer (OPS) and a high magnification imaging system, respectively. The impact of the CNT coating on particle deposition to the bottom wall was studied. Using the experimental data, the particle deposition velocity and relaxation time were compared with numerically simulated results. Finally, using the experimental data, two correlations were generated for penetration as a function of Reynolds numbers for two different particle diameters considered in this study. Figure 1.1 illustrates the work flow of this study.

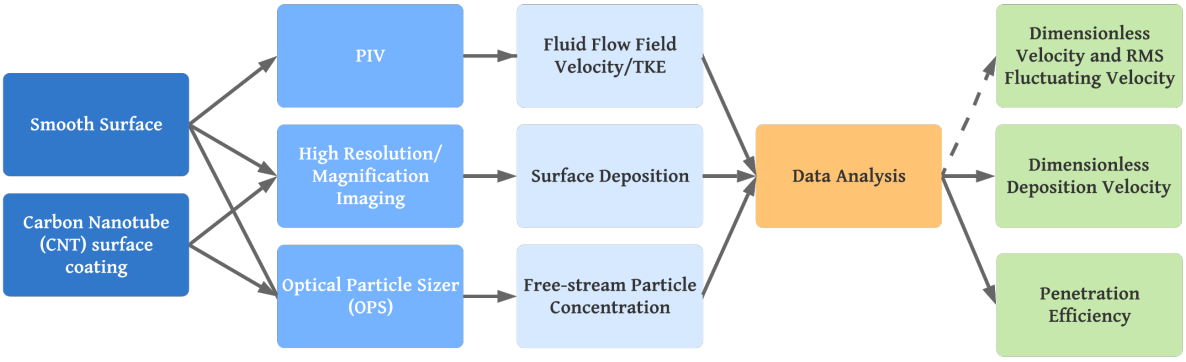

Figure 1.1: Work flow of the experimental study.

Table 1.1: Literature Review

Author (Year)	Channel Geometry (Hydraulic Diameter)	Reynolds Number Range	Particle Type(s)	Particle Diameter (Stokes Number Range)	Experimental Techniques[1,2,3]	Key Findings
Alexander and Coldren (1951)	Circular (4.72 cm)	94,000-278,000	Water Droplets	27 μm (1.4-4.3)	Droplet collection cylinders[1].	• Resistance to particle transport from the bulk flow to duct wall increased from duct center to near the wall region where the majority of resistance was caused by a thin, laminar gas film adjacent to the wall.
Friedlander and Johnstone (1957)	Circular (0.54-2.5 cm)	7,200-30,000	Iron, Aluminum	0.8, 1.32, 2.63 μm (6E-02 - 3.5)	Microscopic measurement[1], isokinetic sampling tube[2].	• For $S^+ <$ sublayer thickness, particle diameter and flow velocity cause rapid increase of transfer coefficient. • In the buffer layer, for $S^+=y^+$, the transfer rate can be calculated using the Reynolds analogy.
Wells and Chamberlain (1967)	Circular (1.27 cm)	2,000-40,000	Aiken Nuclei Tricresyl Phosphate	0.17 μm 0.65-21 μm (3E-04 - 6)	Beta scintillation counter[1], pitot tube[2].	• Filter paper covering the deposition surface increased deposition due to fibers, too small to disturb the viscous boundary layer, protruding in the viscous sublayer, which were able to effectively trap particles. • Deposition rate to natural surfaces could not be successfully predicted since no theory accounts for the nature of the roughness' on a scale too small to affect the airflow.
Sehmel (1968)	Circular (0.53-7.16 cm)	3,000-40,000	Uranine and Uranine-Methylene Blue	1-9 μm (7.5E-03 - 8.1)	Fluorimetric analysis of deposition surfaces and filter loading[1,2].	• In the flow transition regime, deposition velocities were low, of the order of 10-4 cm/sec. • In the turbulent flow regime, radial motion of particles increased causing deposition velocity to increase rapidly with Reynolds number. • Particle re-entrainment occurred at sufficiently high Reynolds number and resulted in decreased deposition velocity.
Farmer et al. (1970)	Circular (1.27 cm)	13,900-28,000	Water Droplets	93-262 μm (3.3 - 559)	Chemical marking on MgO surface coating[1].	• Deposition was inversely proportional to droplet size and air velocity. • The deposition of more easily deposited sizes called "hardening" caused the deposition rate downstream to decrease.
Montgomery and Corn (1970)	Circular (15.3 cm)	5,000-365,000	Uranine-Methylene Blue	0.44-2.61 μm (2.9E-06 - 7.5E-03)	Fluorimetric analysis of surface and filter[1,2].	• Particle dimensionless deposition velocity is strongly dependent upon Reynolds Number. • Electrical charge on the particles appeared to increase aerosol deposition.
Ström (1972)	Circular (1.68 cm)	1,620-5,050	Dioctyl Phthalate	8 μm (1.6E-02 - 5.1E-02)	Tritium contents of surface washings[1], aerosol photometer and tritium content of filters[2].	• The magnitude of the deposition in vertical tubes can be calculated using the theory of Friedlander and Johnstone (1957). • Low Reynolds number deposition in horizontal tubes was higher than in bends, but at higher Reynolds number deposition in bends increased sharply. • A maximum penetration efficiency was demonstrated by testing velocities above and below the "flow of best transmission".
Liu and Illori (1973)	Circular (3.2 cm)	10,000 - 50,000	Uncoated Olive Oil with Uranine-coated Oil Droplets	1.4 - 21 μm (6.72E-03-9.26E-01)	Differential mass by using surface washing[1].	• The trend of increased penetration for decreased particle resulted from inherent inertial effect for a finite particle mass.
McFarland et al. (1991)	Circular (2.66 cm)	3,500 - 6,600	Oleic Acid and Sodium Fluorescein Dissolved in Alcohol	3 - 25 μm (5.19E-05 - 6.8E-03)	Differential mass of tracer[1], isokinetic probe[2].	• Penetration decreased with increasing aerodynamic particle diameter. • Depositional mechanisms such as gravitational settling and turbulent diffusion in the isokinetic probe did not introduce substantial error to the results.

[1]=Deposition related measurements [2]=Concentration related measurements [3]=Flow field related measurements

Table 1.1 Continued

Author (Year)	Channel Geometry (Hydraulic Diameter)	Reynolds Number Range	Particle Type(s)	Particle Diameter (Stokes Number Range)	Experimental Techniques[1,2,3]	Key Findings
Kvasnak et al. (1993)	Rectangular (15.25 x 2.54 cm^2)	15,000	Spherical Glass Particles, Dust components	1 - 10 μm {dust} 5- 45 μm {glass} (1.8E-04-1.46E-02 {glass} 4.28E-06-4.28E-04 {dust})	Surface imaging with image processing[1],isokinetic probe[2].	• Particle diameter was found to be directly proportional to particle deposition rate. • Deposition velocity of compact dust components closely resemble equivalent spherical particles.
Kaftori et al. (1995)	Rectangular (0.32 x 1 m^2)	5,000-14,000	Polystyrene	100 - 900 μm (1.27E-04-2.88E-02)	High-speed video recording of surface[1], 2-D laser doppler anemometry[3].	• Coherent wall structures are dominating factors to particle motion, deposition, and entrainment near solid boundaries in turbulent flows. • Particle entrainment seen as streaks appear to assist deposition by carrying particles in the bulk near wall.
Aluko and Noll (2006)	Rectangular (7.6 x 2.5 cm^2)	63 - 888	Airborne Particles	5 - 100 μm (6.19E-08-3.48E-04)	Differential mass of deposition plate[1], rotary impactor[2].	• Deposition velocities must be described with an enhancement term to Stokes law when inertial and gravitational setting effects are present. • Higher flow velocities allow large airborne particles to remain suspended and counteract gravity. • Gravitational effect on particle velocity lessened with increase in flow velocity regardless of flow direction.
Barth et al. (2013)	Square (10 cm)	8,900-43,100	Polydispersed Graphite Particles	5.3 μm (2.3E-03 - 1.11E-02)	Laser distance sensor for surface layer thickness[1], isokinetic probe with aerodynamic particle sizer[2], stereoscopic particle image velocimetry[3].	• Inertial impaction, turbulent dispersion, and gravitation setting caused a difference between flow field and thickness distributions. • Particle deposition and surface roughness increased as layer thickness increased. • Resuspension cause decreased surface roughness through particle agglomerate removal.
Lin et al. (2014)	Circular (0.8 cm)	1,700-5,120	Particles Generated from the Burning of Incense	50 - 450 μm (3E-05-7.33E-03)	Differential particle number and size distribution using a fast mobility particle sizer (FMPS)[1,2].	• For nano-sized particles, penetration proportional to particle size and inversely proportional to Reynolds number. • Brownian/Turbulent diffusion governed deposition of nano-sized particles.
Zhang et al. (2017)	Rectangular (0.6 x 1.0 m^2)	175,000-417,000	Polydispersed Talcum Powder	11 - 25 μm (1.51E-03-1.86E-02)	Differential mass using a wiping method[1], particle image velocimetry[2,3].	• Concentration stratification along height led to higher floor deposition compared to wall and ceiling, conforming to Rosin-Rammler formula. • Floor deposition increased while wall and ceiling deposition decreased as particle diameter increased.
Dou et al. (2018)	Truncated Icosahedron (1.0 m)	246 - 357	Low/High Density Glass Bubbles	5 - 45 μm (2E-02 - 4.63)	In-house developed planar four-frame particle tracking technique (PTV)[3].	• For a given Reynolds number, particle-pair relative velocity increases with Stokes number at small particle separation distances but decreases with Stokes number at larger particle separation distances, showing the influence of path-history effect and 'inertial filtering' mechanism, respectively.
Gelain et al. (2019)	Circular (0.2 m)	10,00-250,000	DEHS	<1 (<5E-02)	Particle image velocity[2,3].	• The required mixing distance for desired homogeneity and the optimum concentration sampling point was evaluated and validated with a model developed to describe the spatial evolution of tracer concentration with point source injection.

[1]=Deposition related measurements [2]=Concentration related measurements [3]=Flow field related measurements

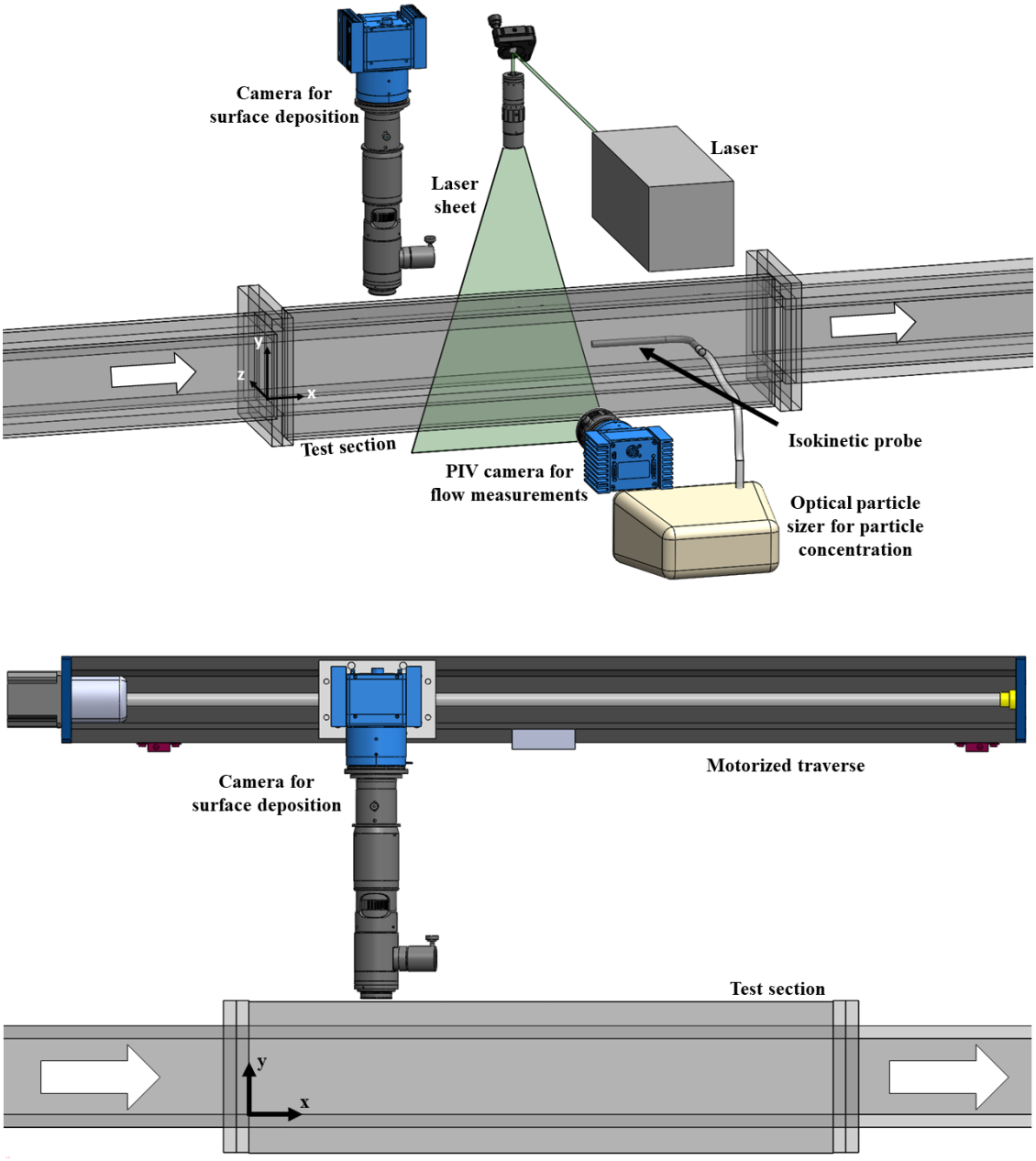

Figure 2.1: Top (a): Experimental facility of horizontal square channel with PIV setup. Bottom (b): Motorized-traverse with a mounted surface deposition camera. Separate traverse into page, for lateral movement (z-direction) is not shown.

To study the flow behavior and particle deposition on the surface of a square duct, an experimental facility was constructed to facilitate experiments. The facility, shown in Figure 2.1, had a cross-sectional area of 7.62×7.62 cm^2 and a total length of 182.88 cm. The facility was divided into three equal sections of 60.96 cm in length. The first section of the facility allowed for flow development. The third section was used for particle filtration and to minimize exit effects. The middle section, i.e. the test section, was used to measure parameters of interest such as the flow velocity, particle concentration, and surface deposition.

The test section was constructed to allow the removal of a single wall. This feature was important because it allows the surface of the test section to be cleaned between tests and modified with the addition of a CNT coating. The facility was connected to an air compressor to adjust the air-flow rates. A hot-wire anemometer was used to measure the inlet velocity at the test section and to determine the volumetric flow rate of the mixture. Equipment constraints require the particle injected air with a supplemental clean air supply in order to reach higher flow velocities. Figure 2.2 (not drawn to scale) illustrates the supplemental clean air supply mixing with the particle-laden air occurring upstream of the first section of the facility. The hot wire anemometer measured flow velocity at the inlet of the middle section.

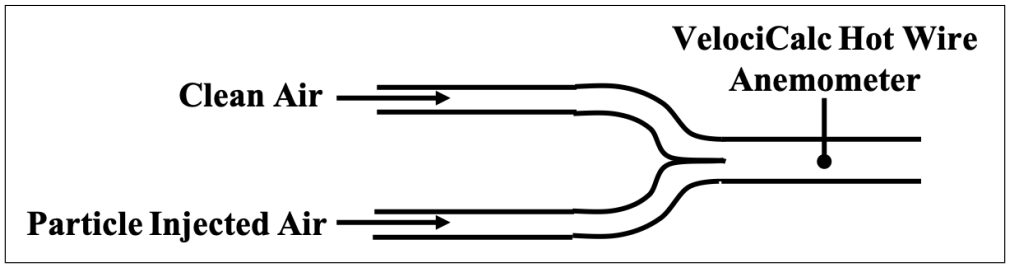

Figure 2.2: Upstream depiction of supplemental air supply used to achieve high flow velocities in the square channel.

2.1 Solid-, Liquid-Aerosol Generation Method

Two methods were used to generate aerosol. To generate solid aerosols with polypropylene microspheres, a constant volume injection method similar to the method used by Barth et al. (2014) was be employed. Using similar injection principles, we fabricated the Solid Particle Injector (SPI) shown in Figure 2.3. The SPI was designed, fabricated, and calibrated in-house using a mass difference calibration technique to measure the injection rate (g/s) for a given delivery speed and injection time (Chavez et al., 2020). The SPI can be broken into three main components:

1. Feeding Belt System
2. Particle Vessel
3. Injection Nozzle

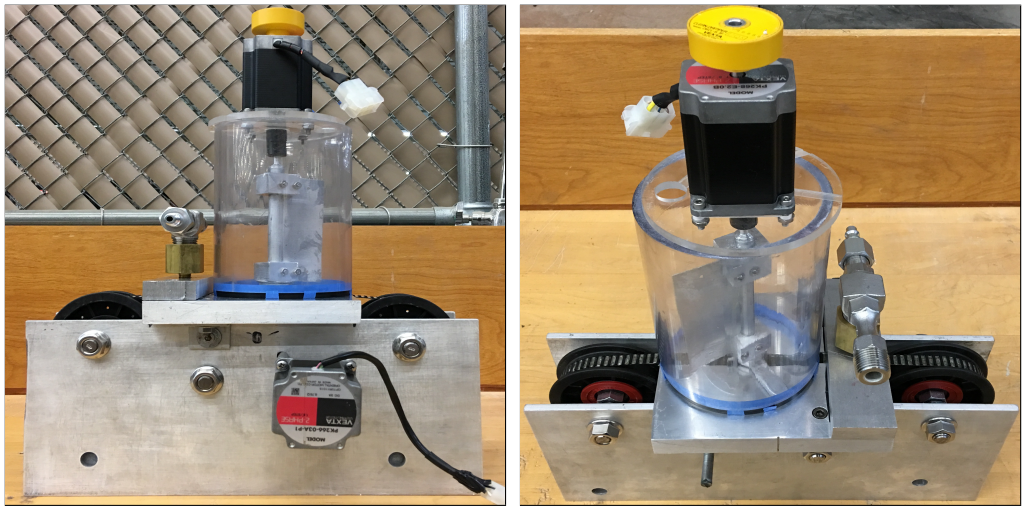

Figure 2.3: Left (a): Back view of the SPI. Right (b): Front view of the SPI.

As shown in Figure 2.4, the feed belt system was comprised of three idle pulleys, a single drive pulley, a feed belt, and a motor. The feeding belt was simply a notched timing belt. A motor was

attached to the shaft connected to the drive pulley such that the speed of the entire feed belt system could be controlled by reducing the rotational speed of the motor using an in-house developed Python script. The volume of the space between the notches on the timing belt was important because each empty space was filled with a fixed volume of particles as the belt moves through the particle vessel.

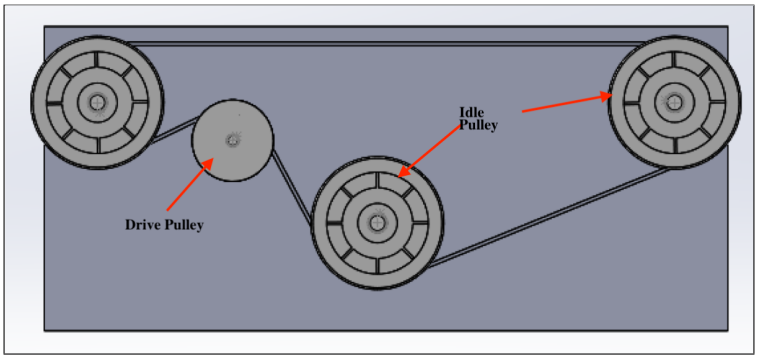

Figure 2.4: Feeding belt system of the SPI. Notches on belt not shown.

As shown in Figure 2.5, the particle vessel was comprised of an acrylic container, a rotating scraper, and a motor. The acrylic container had a port at the top for refilling the vessel with particles. At the bottom of the acrylic container, a surface cut was made upwards into the container. The depth of the surface cut was exactly the height of the notch on the timing belt. Therefore, as the belt passed into the acrylic container, the tops of each notch rubbed against the bottom of the acrylic container. Likewise, as the belt left the acrylic container, the top of the notches of the belt rubbed against the bottom of the container.

The rotating scraper was connected to a motor-driven shaft. The function of the rotating scraper was to ensure the mixing of the bulk of the particles inside the acrylic container and to fill the voids of the belt as it passed along the bottom of the particle vessel. Particles were first pushed into the voids of the belt with the first pass of the scraper. Then, with the second pass of the scraper, extra particles were taken off the top of the belt before the filled spaces left the particle vessel. Through

delicate machining and assembly, a fixed volume of particles was injected to the flow per revolution of the belt system.

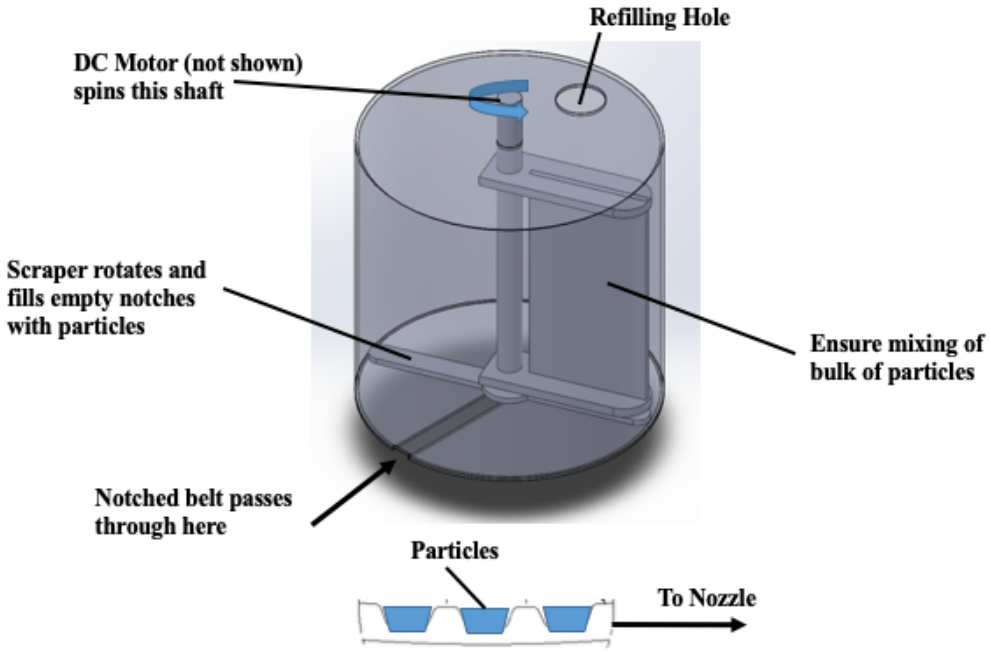

Figure 2.5: Detailed particle vessel schematic of the SPI.

The injection nozzle is shown in Figure 2.6. The function of the injection nozzle was to take in clean, compressed air and then output a solid-aerosol. This was accomplished using a Venturi jet pump. Inside the jet pump, a constricted area was utilized to reduce pressure and provide suction. As air passed through the converging-diverging section of the jet pump, the fluid was ejected at high velocity which created a low pressure region in the throat which acted as a vacuum. This low pressure region in turn drew the particles up from the belt delivery system. The placement of the end of the suction port was chosen such that it hovered less than 2 mm above the top of the notches on the feeding belt. The flow area of the suction port was chosen carefully such that the desired range of flow velocities (i.e., inlet pressures) always produced suction into the Venturi jet pump. Lastly, the particle-laded flow was supplemented with clean air before entering the square channel for higher flow velocities.

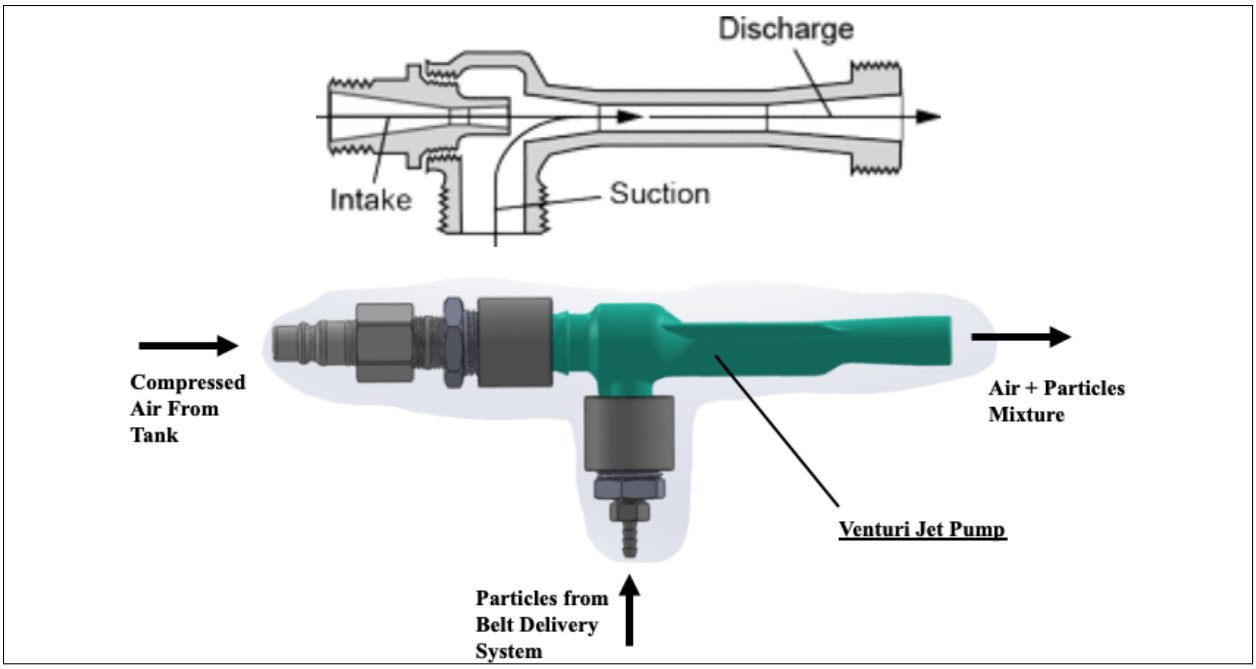

Figure 2.6: Top (a): Venturi jet pump flow schematic. Bottom (b): Assembly of the injection nozzle for the SPI.

Calibration of the SPI was conducted following the calibration setup and procedure recommenced by the manufacturer of the SAG 410. Using a mass balance technique, the mass of particles injected for a given amount of time was found for different injection rates. To vary the injection rate of the SPI, the rotational speed of the drive pulley was varied. The calibration setup shown in Figure 2.7 was comprised of the SPI, a flow channel, a 5μm filter, and a blower. The function of the blower was to minimize backflow upstream of the filter by causing suction downstream of the filter. By marking the initial mass of the filter prior to particle injection and the mass of the filter post-injection, the injection rate could be found for a given injection time.

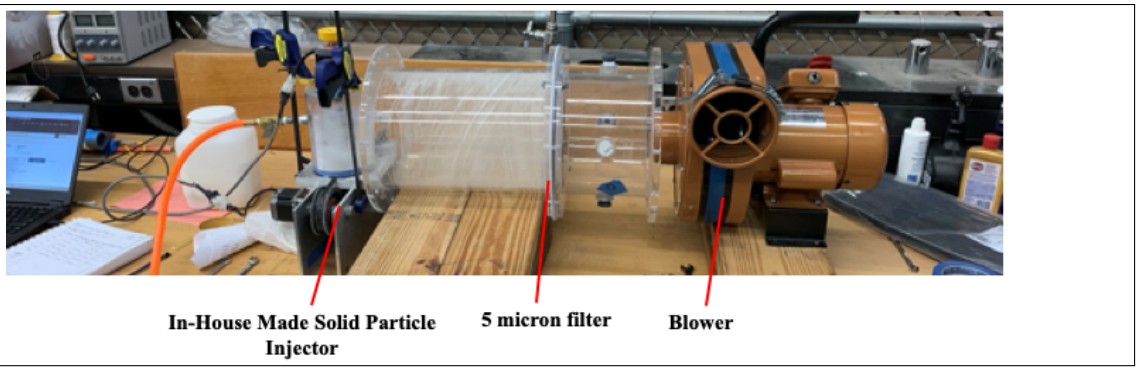

Figure 2.7: SPI calibration setup.

A total of six feeding belt speeds were tested. For each belt speed, the average injection rate was found after a total of 10 trials. Figure 2.8 illustrates the results of the SPI calibration. It can be seen that both the calibration technique and the performance of the SPI was consistent and that the injection rate of the SPI varied linearly with belt speed.

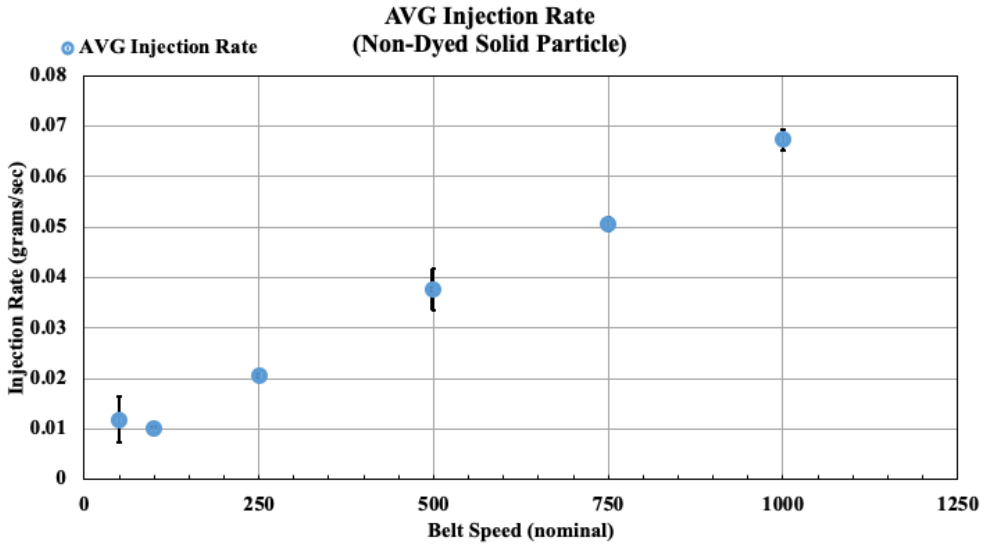

Figure 2.8: SPI injection rate calibration results.

To generate the liquid aerosol with DEHS droplets, a six-jet atomizer (TSI Model 9306) was

used to aerosolize the DEHS fluid (Figure 2.9).

Figure 2.9: TSI Model 9306: Six-jet atomizer used for liquid-aerosol generation.

Due to the OPS measurement device constraints, a valid free-stream concentration measurement could only be taken for an aerosol concentration $\leq 3,000$ particles/cm^3. However, a single jet of the atomizer produced an aerosol concentration of 10^7 particles/cm^3. Therefore, without integrating a dilution system, the optics within the OPS would have been damaged or produced erroneous measurements.

Figure 2.10 is a detailed illustration of the dilution setup. The dilution setup was based off the dilution methods found in aerodynamic particle sizers (APS). The dilution setup consisted of a flow divider where the amount of flow through each branch regulates the amount of dilution applied to the aerosol. In Figure 2.10, there are two bypass lines which circumvent the filtering line. However, only one the bypass lines actually has aerosol flowing through it. The other bypass line is used to gauge the pressure drop across the filter line. By controlling the flow area in the bypass line, the dilution factor can be altered to achieve the desired aerosol concentration to the optical particle sizer.

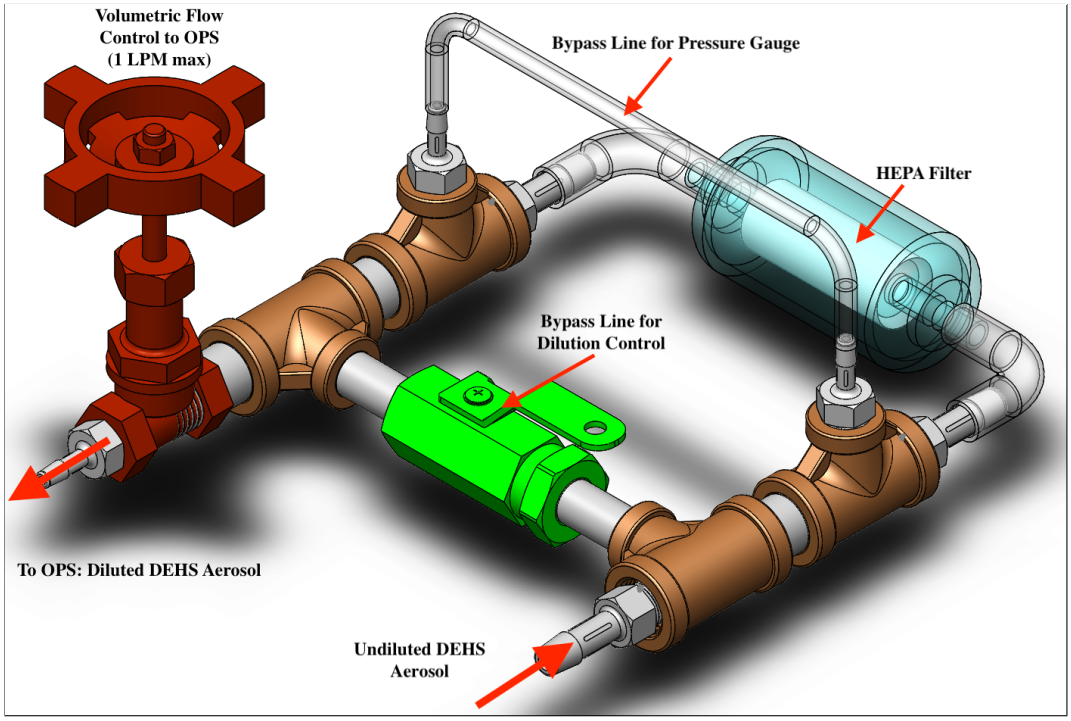

Figure 2.10: Detailed illustration of the dilution setup placed upstream of the OPS and downstream of the sampling probe.

2.2 Experimental Test Conditions

Here, the solid aerosol of polypropylene microspheres is referred to as "solid particle aerosol," whereas the liquid aerosol of DEHS is referred to as "liquid droplet aerosol." The solid particles and liquid droplets used as surrogate particles had a density of 42 kg/m^3 and 910 kg/m^3, respectively. The solid particles had a diameter of $25-50$ μm and the liquid droplets had an average diameter of 2 μm. Surrogate particles with a lower density (42 kg/m^3) represented solid-aerosols and surrogate particles with a higher density (910 kg/m^3) represented liquid-aerosols in the GFR facility. With these two particle diameters, measurements were taken at various flow velocities, and two ranges of Stokes numbers identified as Stk_1 and Stk_2 were obtained because the Stokes number is a function of both flow velocity and particle diameter. Stk_1 refers to the results of solid particle transport, and Stk_2 refers to the results of liquid droplet transport. Table 2.1 summarizes the experimental test conditions of this study.

Table 2.1: Experimental Test Conditions

Particle Type	**Reynolds Number**	**Particle Diameter (Stokes Number)**
Dry expanded polypropylene microspheres	$750 - 7,000$	$25 - 50$ μm Stk_1 = (3.49×10^{-04} - 3.26×10^{-03})
Di-Ethyl-Hexyl-Sebacate		2 μm Stk_2 = ($2.30 \times 10^{-08} - 2.15 \times 10^{-07}$)

3. SCALING APPROACH FOR SURROGATE PARTICLE TRANSPORT

For an accidental scenario due to a break in the primary coolant system of a helium-cooled reactor, fission products may be carried away from the reactor core by the coolant. One potential source during an accident scenario is graphite dust, which has shown affinity for fission products (Zhang et al., 2017). Therefore, it was important to analyze particles within the prototype reactor and scale the particle size and density to be used in the model. To determine the physical properties, such as size and density, of potential surrogate particles that could be used in the test facility, the following dimensionless numbers were crucial.

The Reynolds number was considered to account for the similarities between flow conditions of the prototype and model. The Reynolds number for this scaling approach is defined as

$$Re_f = \frac{U_f \rho_f d_h}{\mu_f} \tag{3.1}$$

where U_f is the fluid velocity, ρ is the fluid density, μ is the fluid dynamic viscosity, and d_h is the hydraulic diameter of the channel.

The Stokes number is a ratio of the characteristic time of a particle to the characteristic time of the flow. The Stokes number was considered to ensure the particles in the flow followed streamlines closely and was defined as

$$Stk = \frac{\rho_{part} d_{part}^2 U_f}{18 \mu_f L} \tag{3.2}$$

where "part" indicates particles, ρ_{part} represents the particle density, d_{part} is the particle diameter, U_f is the fluid velocity, μ_f is the fluid dynamic viscosity, and L is the characteristic length.

Experiments were performed under isothermal conditions (20°C), and the system fluid was air at atmospheric pressure. The ratios of the non-dimensional numbers of the model to those of the prototype were equal to unity to guarantee fluid dynamic similarity. Similarities for the Stokes numbers (Stk_R) between the prototype "p" and model "m" are shown below.

Stokes number similarity Stk_R:

$$Stk_R = \frac{Stk_m}{Stk_p} = \left(\frac{\rho_{part} d_{part}^2 U_f}{18\mu_f L}\right)_m / \left(\frac{\rho_{part} d_{part}^2 U_f}{18\mu_f L}\right)_p \tag{3.3}$$

The properties of helium and graphite dust were assumed for the prototype and applied to the scaling for the experimental facility of the horizontal square channel. From Stokes relation, the particle diameter can be determined as follows:

$$\left(\frac{\rho_{part} d_{part}^2 U_f}{18\mu_f L}\right)_m / \left(\frac{\rho_{part} d_{part}^2 U_f}{18\mu_f L}\right)_p = \frac{\rho_{part,m}}{\rho_{part,p}} \frac{\mu_{f,p}}{\mu_{f,m}} \frac{d_{part,m}^2}{d_{part,p}^2} \frac{L_p}{L_m} \frac{U_{f,m}}{U_{f,p}} \tag{3.4}$$

Considering the similarities for the Reynolds numbers, a similar derivation was performed and substituted into Equation 3.4. The diameter of the particle in the model $d_{part,m}$ was solved algebraically, as follows:

$$\frac{\rho_{part,m}}{\rho_{part,p}} \frac{\rho_{f,p}}{\rho_{f,m}} \frac{d_{part,m}^2}{d_{part,p}^2} \left(\frac{L_p}{L_m}\right)^2 = 1 \rightarrow d_{part,m} = \left(\frac{L_m}{L_p} \sqrt{\frac{\rho_{part,p}}{\rho_{part,m}} \frac{\rho_{f,m}}{\rho_{f,p}}}\right) d_{part,p} \tag{3.5}$$

This could be expressed following the simplified expression:

$$d_{part,m} = \left(\frac{1}{f_{scale}} \sqrt{\frac{\rho_{part,p}}{\rho_{part,m}} \frac{\rho_{f,m}}{\rho_{f,p}}}\right) d_{part,p} = C_{dp} d_{part,p} \tag{3.6}$$

where C_{dp} is a particle diameter coefficient determined by fluid properties and geometric scale. Different reactor prototypes have different potential fission products. Using Equation 3.6, the particle diameter of the scaled model can be modified to accommodate different solid and/or liquid aerosol flows in the prototype. For example, considering graphite dust as the particle in the prototype, $d_{part,m}$ can be accordingly scaled to guarantee similarities between the model and the prototype.

4. DEVELOPMENT AND APPLICATION OF MEASUREMENT TECHNIQUES

4.1 Flow Field Measurement Technique

To acquire the aerodynamic flow fields in the test facility, two-dimensional two-component (2D-2C) PIV measurements were performed. The setup of PIV measurements is shown in Figure 2.1a. The measured flow area was located at the center plane of the test section and illuminated using a laser sheet. The coordinate system of the flow field had the origin chosen at the inlet of the section and along the center plane. The stream-wise, bottom-wall-normal, and lateral directions are denoted for x-, y-, and z-directions, respectively. The time-averaged velocities along the x- and y-directions were denoted as U and V, while u' and v' represent the fluctuating velocities, respectively. The 2D-2C PIV setup included a dual head pulsed laser used for flow field illumination, a charged couple device (CCD) camera used for high resolution imaging, and an oscilloscope used for synchronized triggering. The dual head laser generated 200 mJ beams at a wavelength of 532 nm. The laser beams were adjusted with a combination of cylindrical and spherical lenses to form a laser sheet with a 1 mm thickness. Image pair cross-correlation calculations were made to search for correlation peaks to measure particle displacement. Out-of-plane particle displacements could strongly reduce the correlation peaks thereby reducing the validity of peaks in the correlation map. To reduce the loss of correlation peaks caused by spanwise (out-of-plane z-direction) particle displacement, we followed the procedures suggested in Raffel et al. (2018) to optimize the laser sheet thickness and time-interval between the first and second exposures. The 1-mm laser-sheet thickness was found to be sufficiently thin to guarantee a good particle-image intensity but sufficiently thick to minimize the loss of image correlation due to out-of-plane particle displacements. A CCD 4-MP camera with a pixel size of 5.5×5.5 μm^2 was used to capture the instantaneous image pairs at a sampling rate of 10 Hz. The captured images had a resolution of $2,336 \times 1,752$ pixels. The time interval between the first- and second-image exposures was chosen to be 500 μs that yielded a maximum particle displacement of 10 pixels. The advanced multipass, multigrid robust phase

correlation (RPC) algorithms developed by Eckstein and Vlachos (2009) were applied to process the PIV experimental images. In the PIV processing, four iterations were made. The first pass started at 128×64 pixels and the final pass ended at 32×16 pixels. All PIV interrogation windows had a 50% window overlap, yielding a final distance between two adjacent vectors of 0.73 mm. Particle displacements were calculated from the cross-correlation map, and a Gaussian-peak fit was applied for subpixel accuracy (Raffel et al., 2018). Erroneous particle displacements were detected using statistical validations and a median filter (Westerweel, 1994), based on the standard deviations of neighboring vectors, was used to filter out spurious vectors. The resultant gaps were then filled by velocity interpolation.

4.1.1 Flow Field Measurement Technique Calibration

Prior to collecting flow field images, the following images shown in Figure 4.1 were taken in order to convert the flow field velocity data into physical units. An image with a ruler was used to determine the stream-wise location which the flow field data was taken. The image with the LaVision calibration target was used to determine the pixel-to-physical coordinate conversion ratio used in PIV post-processing.

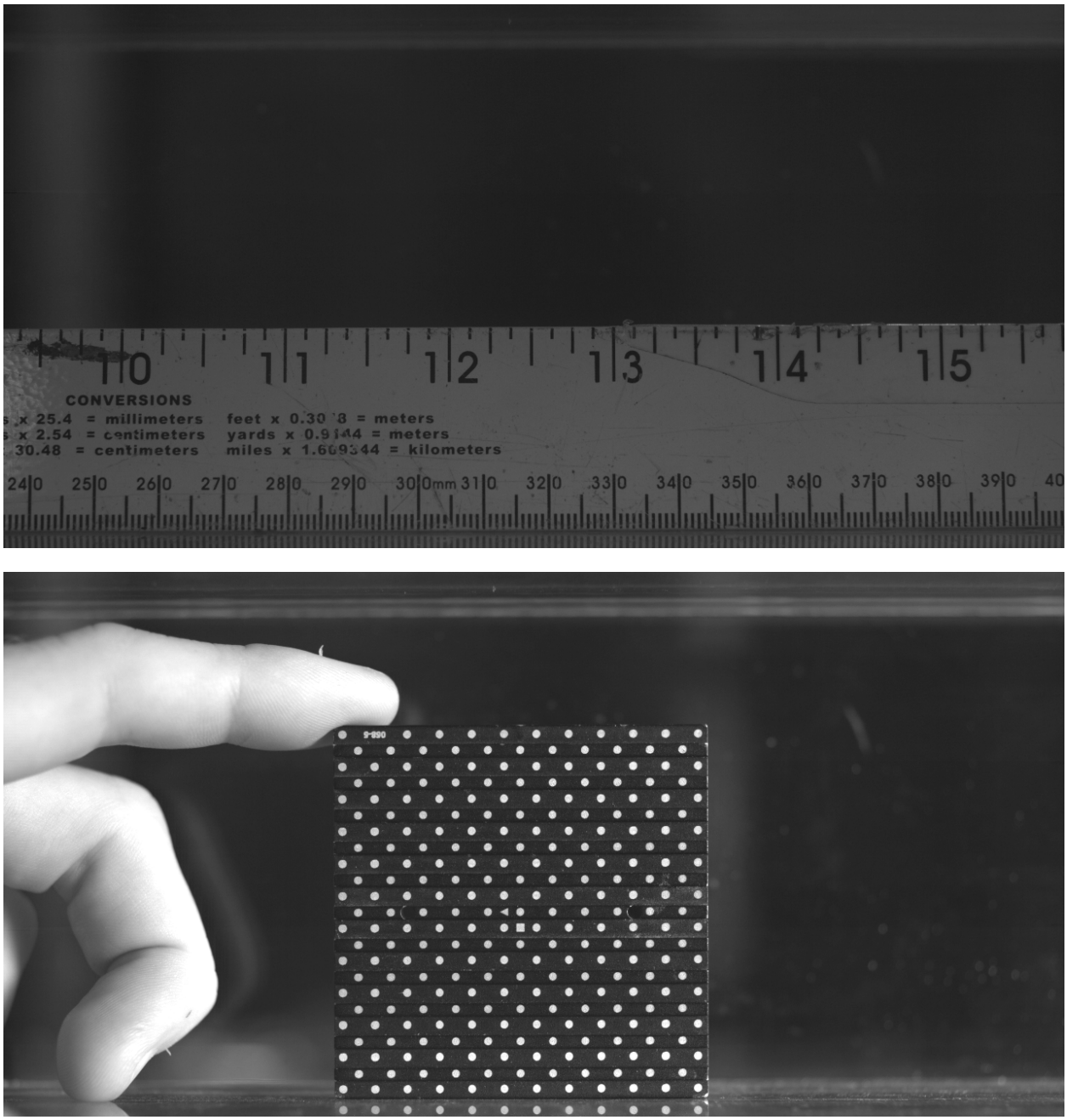

Figure 4.1: Top (a): Ruler image used to determine stream-wise location of flow field measurement. Bottom (b): LaVision calibration target image used to determine pixel-to-physical coordinate conversion ratio.

4.2 Surface Deposition Measurement Technique

Images of the bottom surface of the test section were captured to obtain the particle deposition rate and the stream-wise/lateral deposition distribution using a high magnification imaging system and a motorized-traverse system, as shown in Figure 2.1b. Images of the particle surface deposition were captured using an 8-MP CCD camera (Imperx B3320) with a maximum resolution of $2,458 \times 3,312$ pixels and a pixel size of 5.5×5.5 μm^2. The camera was mounted with a 12X zoom lens with 3-mm fine focus (ThorLabs MVL12X3Z). Additional lens attachments were added to achieve a working distance of 108 mm, which allowed the entire imaging system to remain outside the test section and provided the freedom to capture images from all locations of the bottom wall of the test section using the motorized-traverse system. The lens selection criteria were driven by the required working distance and depth of field; however, additional factors such as the matching pixel size and resolving limit were considered to capture detailed images of both particle types. The depth of the field ranged from 0.09 mm to 2.54 mm, and the resolving limit ranged from 4.44 μm to 23.80 μm. A summary of the magnification details of the final lens combination can be found in Table 4.1. To convert the surface depositon images to physical dimensions a calibration image using a LaVision target was taken (Figure 4.2). To illuminate the test section, a 400 W, $18,000$ lm LED light panel was used, which spanned the length of the test section. For the tests performed in this study, the surface deposition camera operated at 8 Hz and 0.08 Hz. The higher frequency was used to collect images while both the solid and liquid aerosols were flowing through the square channel. The lower frequency was applied during the automated surface scans. The low capture frequency of the surface scans allowed time for the motorized-traverse to travel 1 mm in the stream-wise or lateral direction and allowed small vibrations to dampen before capturing a clear, focused image.

Table 4.1: Optical Magnification Details of Surface Deposition Camera Lens Combination

Working Distance	**System Magnification (Low-High)**	**Depth of Field (Low-High)**	**Resolving Limit (Low-High)**
108 mm	0.44 - 5.25	2.55 mm - 0.09 mm	23.80 μm - 4.44 μm

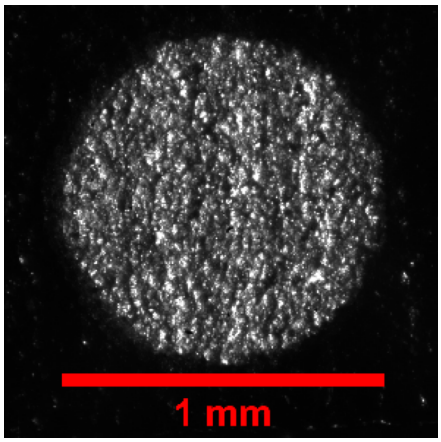

Figure 4.2: LaVision calibration target image taken by the high magnification imaging system. Used to determine conversion ratio of pixel-to-physical dimension of the surface deposition images.

For measurement of the deposition rate, images had to be captured while the solid or liquid aerosols flowed through the channel. Prior to initializing particle injection, the flow was allowed to completely develop in the channel and reach a steady flow condition. The surface deposition camera and the aerosol generation method were started simultaneously once a steady flow condition was met. The surface properties were altered by attaching a carbon nanotube sheet (Miralon) to the surface of the channel. The sheet thickness was 20μm, and the channel surface was assumed to be aerodynamically smooth with and without the addition of the CNT sheet. For each particle

type, a total of 10 different flow velocities were tested, and each test was repeated a minimum of three times. Between each test, all three sections of the channel were cleaned to remove any particles deposited on the surface. Likewise, the deposition experiments to the CNT surface required removal of the particle laden sheet and the subsequent installation of a clean CNT sheet between each test. The surface was imaged when the particles simultaneously deposited to calculate the instantaneous deposition rates, which statistically improved the calculated average deposition rate.

The deposition rate was obtained using a series of image post-processing steps, which involved using in-house MATLAB codes and ImageJ to facilitate the image filtering (Schneider et al., 2012; Fischer et al., 2018). Uneven illumination in the raw image was rectified by image division with a flat field image. This process is shown in Figures 4.3 and 4.4. Shown in Figure 4.4, it can be seen that flat field division also eliminated specs of dust on the camera sensor. Dust was identified in the early stages of the experimental study when every image of the particles contained the same pattern of dark spots left by dust. After careful cleaning of the camera lens and sensor, the flat field correction step was always the first image transformation done.

Lastly, Figure 4.5 illustrates the transformation of a raw image into an image which has outlined each individual particle cluster. To summarize, image transformations included image division, thresholding, followed by binarization. By thresholding the uniformly illuminated image, a binary image was produced. The process of binarization converts the range of pixel intensities from a value ranging from $0 - 255$ for an 8-bit image to a value of either zero or one. The binary image was used to calculate the area of the image covered with particles or without particles.

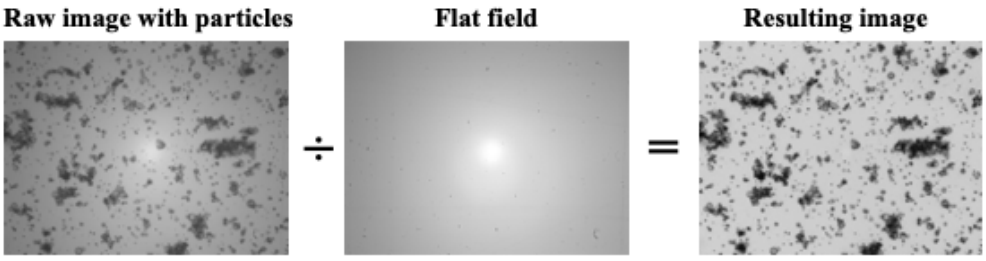

Figure 4.3: Flat field image correction used to rectify uneven illumination and dust on camera lens/sensor.

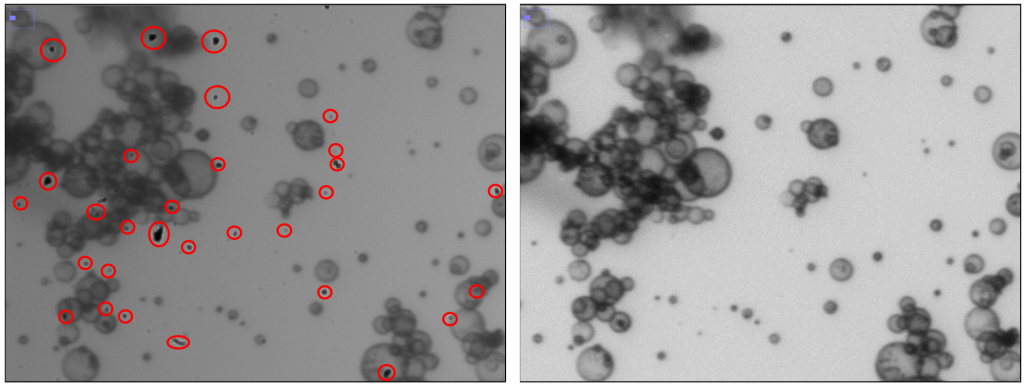

Figure 4.4: Left (a): Raw image before flat field correction, dust on lens circled in red. Right (b): Raw image after flat field correction illustrating the elimination of dust in the image.

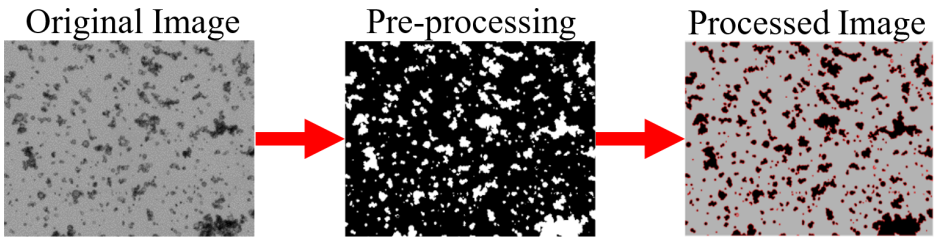

Figure 4.5: Particle deposition image processing

Deposition distribution scans were taken using a motorized-traverse to automate scanning of the bottom wall of the test section for the shaded areas seen in Figure 4.6a. Images of the bottom surface were captured, post-processed, and stitched together to reveal the spatial deposition concentration as a function of the stream-wise and lateral directions, denoted as the x- and z-directions, respectively. A sample of the reconstructed image is shown in Figure 4.6b. Reconstructed images were then utilized to map out the surface concentration of particles for a given location in the x- and z-directions.

The layout of the deposition scanning grid in Figure 4.6a was designed to capture any discernible features of the deposition rate in the stream-wise and lateral directions. Numerous computational studies (Choi et al., 2019; Phares and Sharma, 2006; Sharma and Phares, 2006; Gavrilakis, 1992) have simulated the turbulent flow in a square duct and have shown a possible deposition enhancement caused by secondary vortices located in the corners and/or the turbophoretic force. Figure 4.7 depicts the direction of these secondary vortices which may pull particles from the bulk flow and towards the channel corners. Therefore, the spatial particle concentration at the wall along the stream-wise centerline was scanned because it was proposed that this region is less affected by the presence of secondary corner vortices, thereby isolating the stream-wise scan from the effect of corner vortices on the deposition rate. In contrast, lateral scans in the channel were performed to measure the enhancement in deposition, if any, caused by corner vortices.

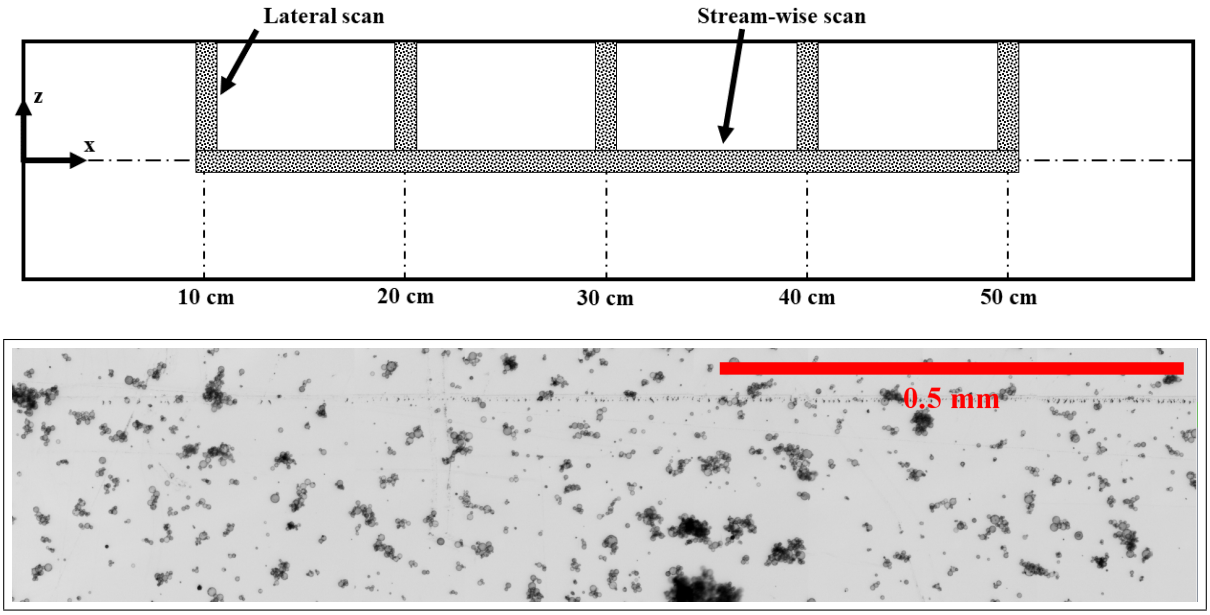

Figure 4.6: Top (a): Bottom surface deposition scanning grid showing stream-wise (x) and lateral (z) regions used to obtain a deposition distribution. Bottom (b): Reconstructed images of a particle surface deposition over 0.27 mm $\times$ 1.28 mm (410 pixel $\times$ 1917 pixel). The image shown is a small portion of the stream-wise scan in the x-direction.

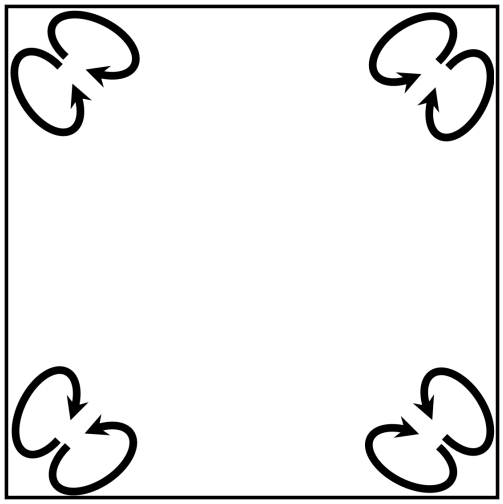

Figure 4.7: Secondary vortices special to rectangular channel flow.

4.3 Particle Concentration Measurement Technique

Similar to previous studies that have probed the flow to measure particle concentrations, this study utilized an isokinetic sampling probe to collect a small volume of aerosols for analysis. As can be seen in Figure 2.1a, the isokinetic probe was placed in the center of the channel using a sealed port hole drilled into the removable plate of the test section. Once gathered by the probe, the sampled aerosol was analyzed using an optical particle sizer (Figure 4.8). The OPS (TSI 3330) was capable of measuring the size (i.e. diameter) of the particle by correlating laser-diode-pulse lengths from the photo detector to its size. Based on the particle size (i.e., pulse length), the OPS counted and placed the count into one of sixteen bins. After sampling for one minute, a concentration distribution based on the 16 different bins was saved along with the cumulative concentration of all bins for a single test. OPS could only measure the concentration of particles sizes between 0.3-10 μm. Therefore, this device was only used to measure the free-stream concentration of particles using DEHS droplets because the size distribution of these particles was within the 0.3-10 μm range. The cumulative concentration measured at the inlet and outlet of the test section was used to report the penetration efficiency (Section 5.2) for the DEHS droplets.

Figure 4.8: Optical particle sizer used to measure free-stream particle concentration of the liquid aerosol.

For isokinetic conditions to be met, the average velocity inside the duct should be equal to the velocity inside the sampling probe. To achieve this condition for various flow velocities, the cross-sectional area of the sampling probe was sized accordingly such that the ratio of duct to probe velocities was equal to unity. For instance,

$$\frac{\text{Probe Volumetric Flow Rate}}{\text{Probe Flow Area}} = \frac{\text{Duct Volumetric Flow Rate}}{\text{Duct Flow Area}} \tag{4.1}$$

4.4 Surface Modifications

To investigate filtration effects of surface coatings, a pre-/post-test was conducted by comparing the deposition results a smooth surface to a surface coated with a CNT sheet. The carbon nanotube sheet had a thickness of 20 μm and can therefore be considered a surface coating. It was assumed the channel remained aerodynamically smooth with this modification. In Figure 4.9, an image of the CNT microstructure shows the interwoven pattern of the CNT sheet. Also, sample images showing the solid particle deposited onto the two surfaces is shown.

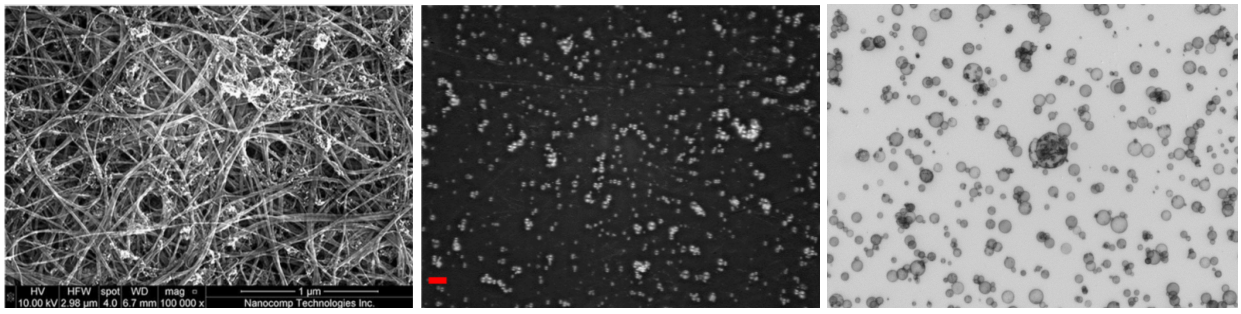

Figure 4.9: Left: CNT microstructure. Middle: Solid particle deposited on CNT surface. Right: Solid particle deposited on smooth surface.

5. DATA REDUCTION

5.1 Calculation Method for Dimensionless Particle Deposition Velocity

The average deposition velocity of the particles over the duration of the injection time was calculated as a ratio of the particle flux to the wall and the free-stream concentration, as follows:

$$u_d = \frac{J_{avg}}{C_0} \tag{5.1}$$

where J_{avg} is the average particle flux to the wall ($\#/m^2 \cdot s$) and C_0 is the free stream aerosol concentration ($\#/m^3$). Equation 5.1 assumes that particles are uniformly deposited on the channel surface. The particle flux was experimentally determined by counting the number of particles deposited in the imaging area as a function of time. The instantaneous particle flux J_i ($\#/m^2 \cdot s$) was determined using the following equation:

$$J_i = \frac{N_{dep,i}}{A_{img} t_i} \tag{5.2}$$

where $N_{dep,i}$ ($\#$) is the instantaneous number of particles deposited on the wall in the image, A_{img} (m^2) is the area of the image captured with the surface deposition camera, and t_i (s) is the time after particle injection (Kvasnak et al., 1993). The average particle flux to the wall was then averaged using all images taken during the duration of the total injection time as follows:

$$J_{avg} = \sum_{i}^{n} \frac{N_{dep,i}}{A_{img} t_i} \tag{5.3}$$

where n is the final image taken in the injection process. It was difficult to determine the number of individual particles detected and counted on the image with the polypropylene microspheres because of the clustering of individual particles. To rectify this issue, the value of N_{dep} was obtained by dividing the total area of the image covered by particles A_{part} (m^2) by the average

cross-sectional area of a single particle A_{avg} (m^2).

$$N_{dep} = \frac{A_{part}}{A_{avg}} \tag{5.4}$$

The non-dimensional particle deposition velocity was then calculated using Equation 5.5, where u^* is the friction velocity.

$$u_d^+ = \frac{u_d}{u^*} \tag{5.5}$$

For cases where PIV data were available, the friction velocity u^* was calculated using Equation 5.6. τ_w is the wall-shear stress and was calculated using Equation 5.7.

$$u^* = \sqrt{\frac{\tau_w}{\rho_f}} = \sqrt{\nu_f \frac{\partial U}{\partial y}} \tag{5.6}$$

$$\tau_w = \mu_f \left. \frac{\partial U}{\partial y} \right|_{y=wall} \tag{5.7}$$

The velocity gradient $\partial U/\partial y$ was determined at the wall and computed at the first PIV grid point in the vicinity of the wall. Likewise, the non-dimensional wall distance y^+, defined as

$$y^+ = \frac{y u^*}{\nu} \tag{5.8}$$

was calculated to illustrate the flow regimes near the wall.

For cases in which the PIV data were not available, Equation 5.9 was used to estimate the friction velocity u^*. The friction factor f was computed using the Blasius correlation (Equation 5.10) corrected for non-circular ducts by replacing diameter with the equivalent diameter (Liu and Agarwal, 1974; Anand and McFarland, 1989; McFarland et al., 1991):

$$u^* = \sqrt{\frac{f}{2}} \bar{u} \tag{5.9}$$

$$f = \frac{0.316}{4Re^{\frac{1}{4}}} \tag{5.10}$$

where $\bar{u}$ is the mean fluid flow velocity measured using a hot-wire anemometer, and Re is the fluid flow Reynolds number using the hydraulic diameter of the flow channel.

The model for empirically estimating the non-dimensional particle deposition rates in turbulent flows was adopted from the study of Wood (1981b) modified by Kvasnak et al. (1993) to compare against the experimental data. Wood's model was defined as

$$u_d^+ = 0.057Sc^{-2/3} + 4.5 \times 10^{-4}\tau_{part}^{+2} + \tau_{part}^+ g^+ \tag{5.11}$$

where Sc is the particle Schmidt number, g^+ is the non-dimensional acceleration due to gravity, and τ_{part}^+ is the non-dimensional particle relaxation time. In Equation 5.11, the $1st\ Term$ numerically described the effect of Browian diffusion, the $2nd\ Term$ described the effect of eddy-impaction, and the $3rd\ Term$ described the effect of gravitational sedimentation (Kvasnak et al., 1993; Sippola and Nazaroff, 2004). The particle Schmidt number is defined as

$$Sc = \frac{\nu}{D_p} \tag{5.12}$$

where D_p is the particle mass diffusivity and is defined with Einstein's equation as

$$D_p = \frac{kT}{3\pi\mu_f d_{part}} \tag{5.13}$$

where k is the Boltzmann's constant, T is the absolute temperature, μ_f is the dynamic viscosity of the fluid, and d_{part} is the particle diameter. The non-dimensional acceleration due to gravity was defined as

$$g^+ = \frac{\nu g}{u^{*3}} \tag{5.14}$$

The non-dimensional particle relaxation time τ^{+}_{part}, assuming Stokes flow, was given by

$$\tau^{+}_{part} = \frac{d^{2}_{part} u^{*2} \rho_{part}}{18 \nu^{2} \rho_{f}} \tag{5.15}$$

where the condition for Stokes flow was met by ensuring the particle Reynolds number was less than one ($Re_{part} < 1$). The particle relaxation time characterized the time required for a particle to adjust its velocity to the fluid flow velocity. The Reynolds number of the particle was given by

$$Re_{part} = \frac{d_{part} u_{rel}}{\nu_{f}} \tag{5.16}$$

where u_{rel} is the relative velocity of the particle to the fluid (Wood, 1981b).

5.2 Calculation Method for Penetration Efficiency

Herein, two different types of aerosols, i.e., solid particles with Stk_1 and liquid droplets with Stk_2, were considered. Each of these two particle cases requires two different measurement techniques to calculate the particle penetration efficiency (P). To calculate the penetration efficiency for the polypropylene microspheres (P_{Solid}), the ratio of the number of particles leaving the duct N_{out} and the number of particles injected into the duct N_{in} was estimated using

$$P_{Solid} = \frac{N_{out}}{N_{in}} = \frac{N_{in} - N_{dep}}{N_{in}} \tag{5.17}$$

where the calculated number of particles injected into the channel N_{in} was found using

$$N_{in} = \frac{\dot{m}_{SPI} t_{injection}}{\rho_{part} V_{part}} \tag{5.18}$$

The injection rate (g/s) $\dot{m}_{SPI}$ of the SPI was a known quantity after calibration of the SPI. The total particle injection time was represented by $t_{injection}$ and V_{part} was the average volume of a single

particle. Substituting Equations 5.4 and 5.18 into Equation 5.17, we get

$$P_{Solid} = \frac{\frac{\dot{m}_{SPI} t_{injection}}{\rho_{part} V_{part}} - \frac{A_{part}}{A_{avg}}}{\frac{\dot{m}_{SPI} t_{injection}}{\rho_{part} V_{part}}} \tag{5.19}$$

To calculate penetration efficiency of liquid DEHS droplets (P_{Liquid}) at different flow velocities, Equation 5.20 was used:

$$P_{Liquid} = \frac{c_{out}}{c_{in}} \tag{5.20}$$

where c_{out} and c_{in} were the free stream concentrations sampled at the inlet and outlet, respectively, of the test section using an isokinetic sampling probe connected to an optical particle sizer.

6. UNCERTAINTY ANALYSIS

6.1 Uncertainty of the PIV Technique

The uncertainty sources associated with the measurement of particle displacement and the calculated velocity include the particle-fluid behavior and calibration along with random errors in velocity vectors. To minimize the error due to particle-fluid behavior, the Stokes number of the particle was maintained at Stk < 0.1. The particle diameters were carefully chosen to be sufficiently large to produce good quality images but also to maintain a small enough Stk number. The calibration images were captured using a high-precision LaVision target with known dimensions. The particle velocity can be expressed simply as

$$U_P = \alpha \frac{\Delta X}{\Delta t} \tag{6.1}$$

where ΔX is the particle displacement in pixels, and α is the image magnification factor. The percent uncertainty in the velocity can be expressed as follows:

$$U_{\%U_p} = \sqrt{U_{\%\alpha}^2 + U_{\%X}^2 + U_{\%t}^2} \tag{6.2}$$

where $U_{\%\alpha}$, $U_{\%X}$, and $U_{\%t}$ are the percent uncertainties associated with the magnification factor, particle displacement, and time interval, respectively. $U_{\%U_p}$ was estimated to be less than 2% of the mean velocity for all velocity vectors calculated. This method, described by Sabharwall et al. (2013), was used to estimate the uncertainties from the PIV measurements.

In this study, the PIV technique only allowed the measurements of two velocity components *u* and *v*. Therefore, the turbulent kinetic energy is defined as

$$TKE = 0.5(\bar{u'^2} + \bar{v'^2}) \tag{6.3}$$

where the over-bar represents the time-averaging operator. The uncertainty of the TKE is defined as

$$U_{TKE} = (R_{uu}^2 + R_{vv}^2)^{1/2}(1/(2N))^{1/2} \tag{6.4}$$

where R_{uu} and R_{vv} represent the Reynolds normal stress for the u and v components, respectively. The percent uncertainty of the TKE was conservatively estimated to 4.3%.

6.2 Uncertainty of Deposition Velocity and Penetration Efficiency

The uncertainty associated with the calculation of the dimensionless particle deposition velocity was dependent on the method used to calculate the friction velocity. When the friction velocity was calculated from PIV measurements, Equation 6.5 was used to estimate the percent uncertainty of the reported values, where $U_{\%A_{part}}$, $U_{\%C_0}$, $U_{\%\alpha}$, $U_{\%X}$, $U_{\%t}$ are the percent uncertainties associated with the particle area in an image, particle concentration, magnification factor, particle displacement, and time interval, respectively.

$$U_{\%u_d^+} = \sqrt{U_{\%A_{part}}^2 + U_{\%C_0}^2 + U_{\%\alpha}^2 + U_{\%X}^2 + U_{\%t}^2} \tag{6.5}$$

In contrast, in cases when the friction velocity was estimated using the Blasius correlation, Equation 6.6 was used to estimate the percent uncertainty of the reported values. $U_{\%f}$, $U_{\%Re}$, and $U_{\%\bar{u}}$ are the percent uncertainties associated with the friction factor, Reynolds number, and flow velocity, respectively.

$$U_{\%u_d^+} = \sqrt{U_{\%A_{part}}^2 + U_{\%C_0}^2 + U_{\%f}^2 + U_{\%Re}^2 + U_{\%\bar{u}}^2 + U_{\%\alpha}^2} \tag{6.6}$$

The dimensionless particle deposition velocity percent uncertainty $U_{\%u_d^+}$ was estimated to be 8.23% of the mean velocity for cases in which PIV data were available and 17.36% for cases in which PIV data were unavailable.

The percent uncertainty of the penetration efficiency associated with the polypropylene particles ($U_{\%P_{Solid}}$) was estimated using Equation 6.7, where $U_{\%\dot{m}_{SPI}}$, $U_{\%t_{injection}}$, and $U_{\%d_{part}}$ are the percent uncertainties associated with the particle injection rate, particle injection time, and particle

diameter, respectively.

$$U_{\%P_{Solid}} = \sqrt{U^2_{\%\dot{m}_{SPI}} + U^2_{\%t_{injection}} + U^2_{\%d_{part}} + U^2_{\%A_{part}} + U^2_{\%\alpha}} \tag{6.7}$$

The percent uncertainty of the penetration efficiency associated with the DEHS droplets ($U_{\%P_{Liquid}}$) was estimated using Equation 6.7, where $U_{\%c_{in}}$ and $U_{\%c_{out}}$ are the percent uncertainties associated with the aerosol concentrations.

$$U_{\%P_{Liquid}} = \sqrt{U^2_{\%c_{out}} + U^2_{\%c_{in}}} \tag{6.8}$$

The percent uncertainty of the polypropylene particle penetration efficiency $U_{\%P_{Solid}}$ was estimated to be 7.66%, and the percent uncertainty of the DEHS droplet penetration efficiency $U_{\%P_{Liquid}}$ was estimated to be 21.71%. Table 6.1 summarizes the reported values of percent uncertainties.

6.3 Uncertainty of Spatial Deposition Concentration

The accuracy of the deposition concentration is a combination of the accuracy of the detected particle area and the area of the image. The contribution of scaling accuracy when converting from pixel units to physical units cancels out when computing deposition concentration A_{part}/A_{step}. Also, the area of the step is a constant since the image size does not change. Therefore, the uncertainty of the deposition concentration is simply the uncertainty of the detection method used to find A_{part} which is $\pm 0.0107\% \times$ Spatial Deposition Concentration. This results in a negligible error associated with measuring A_{part} and reporting the Spatial Deposition Concentration.

Table 6.1: Summary of Percent Uncertainties for Calculated Quantities

Calculated Quantity	**Percent Uncertainty**
U_p **from PIV**	<2%
TKE **from PIV**	4.3%
u_d^+	8.23-17.36%
P_{Solid}	7.66%
P_{Liquid}	21.71%

7. RESULTS AND DISCUSSION

7.1 Flow Field Measurement Results from PIV

Statistical results from PIV are presented here for selected experimental conditions. To illustrate the mean velocity vector field and color contour of the normalized velocity magnitude, results for the DEHS droplets are presented for PIV data collected at the test section inlet and the middle of the test section. The data taken at the middle of test section corresponded to Reynolds numbers of Re = $3,600$ and Re = $6,100$. To demonstrate the variation in the channel velocity profile as a function of stream-wise location, the normalized velocity magnitude of the stream-wise velocity component taken from the color contours is plotted in Figure 7.2 from different locations in the stream-wise direction. The magnitudes of the turbulent kinetic energy (TKE) measured with DEHS droplets for Re = $3,600$ and Re = $6,100$ are presented as color contours in Figure 7.3. The data taken at the inlet of test section corresponded to lower Reynolds numbers ranging from Re = $1,100$ to Re = $2,500$. The purpose of collecting PIV data at the inlet of the test section was to visualize any entrance effects upstream from the primary measurement location. Table 7.1 summarizes the details of the results presented in Section 7.1

Table 7.1: Overview of PIV Results

Result Type	**Reynolds Number**	**Location (X in mm)**	**Particle Type**
Velocity Vector Field Normalized Velocity Magnitude Contour TKE Color Contour	$3,600, 6,100$	Middle $X = 232 - 326$	Liquid
Near Wall Results	$3,500 - 5,900$	Middle $X = 232 - 326$	Liquid Solid
Velocity Vector Field Normalized Velocity Magnitude Contour	$1,100 - 2,500$	Inlet $X = 13 - 165$	Liquid

7.1.1 PIV Results Taken at the Middle of the Test Section

The mean velocity vector fields for both Reynolds numbers (Re = $3,600$ and Re = $6,100$) are shown in Figure 7.1. The time averaged velocity fields were found to be consistent throughout the measurement area. The uni-directional velocity fields represent the flow conditions in which the entrance and exit effects of the test section did not impact the PIV measurement area. With respect to the color contour of the velocity magnitude, the velocity magnitude was observed to decrease when approaching the walls for the flow channel, thus indicating the no-slip flow condition at the geometric flow boundaries.

To verify the flow condition was fully developed, velocity profiles taken at Re = 3,600 and Re = 6,100 for DEHS droplets are shown in Figure 7.2. For both conditions, the velocity profiles were found to remain unchanged in the stream-wise direction. Four stream-wise locations were chosen to numerically describe a velocity profile's proximity to achieving the fully developed flow condition. The velocity profile at the furthermost stream-wise location (x = 326 mm) was considered as the fully developed velocity profile. Then, the percent differences were calculated by comparing profiles at x = 256 mm, x = 279 mm, and x = 303 mm to the furthermost profile. The average percent difference between velocity profiles with respect to the furthermost stream-wise location was less than 0.1%.

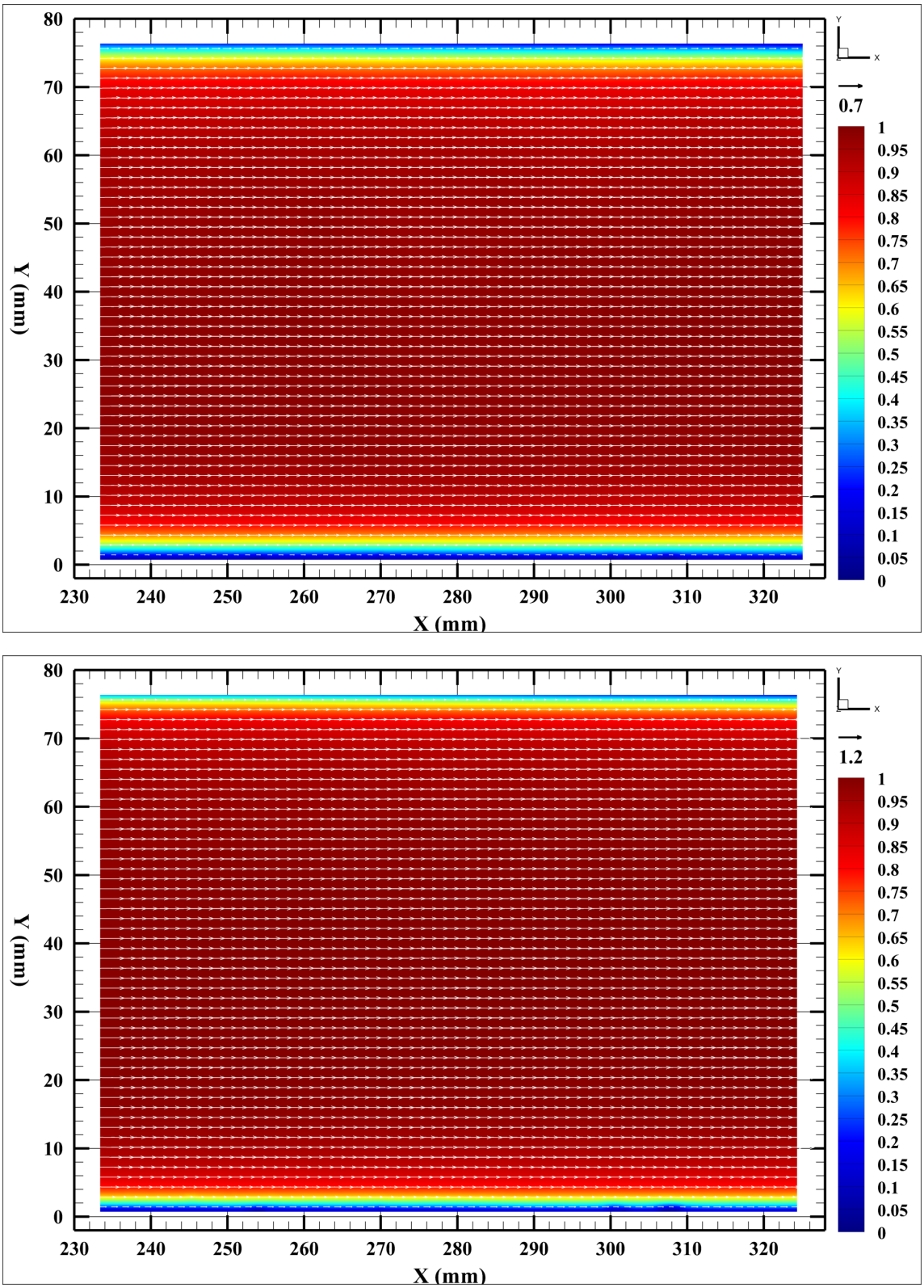

Figure 7.1: Mean velocity vector fields and color contour of normalized velocity magnitude. Top (a): Re = $3,600$, Bottom (b): Re = $6,100$.

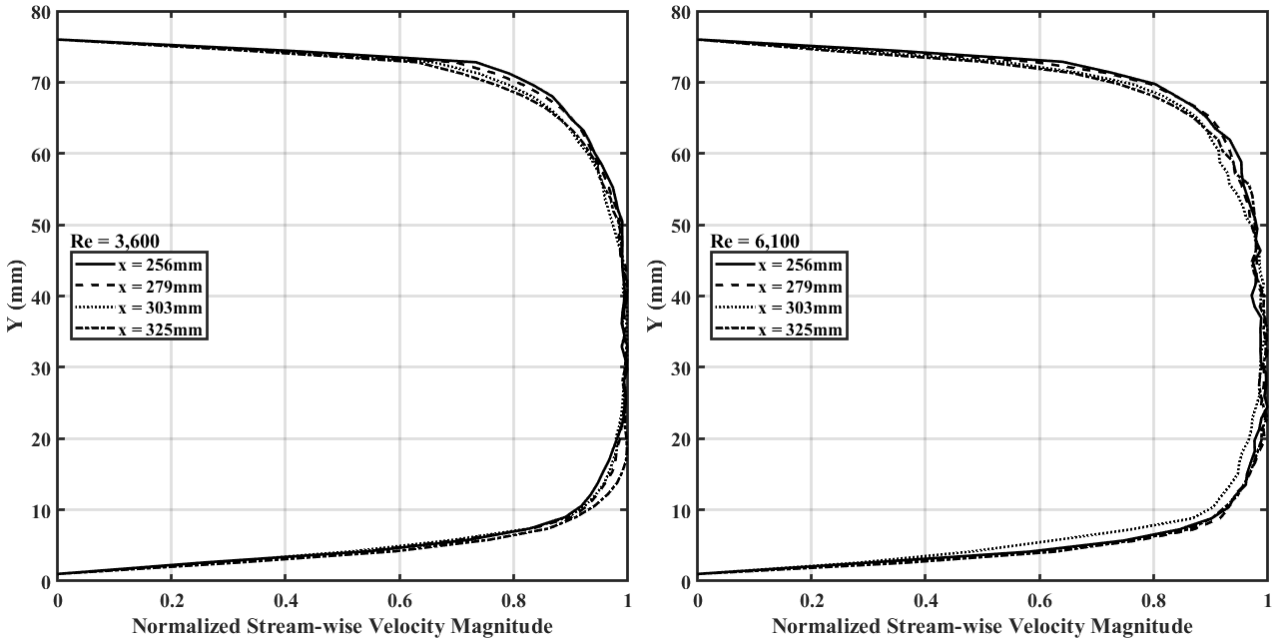

Figure 7.2: Normalized velocity profiles along various stream-wise locations. Left: Re = $3,600$, Right: Re = $6,100$.

The magnitudes of the turbulent kinetic energy measured with DEHS droplets for Re = 3,600 and Re = 6,100 are presented as color contours in Figure 7.3. The color contours of the TKE magnitude for both flow conditions spatially illustrate the degree of mixing within the channel. At Re = 3,600, the flow was found to not be fully turbulent because the magnitude of the TKE was not uniform in the channel. In contrast, with an increase in flow velocity, as seen for Re = 6,100, the TKE was uniform throughout the majority of the channel, denoting a fully turbulent flow.

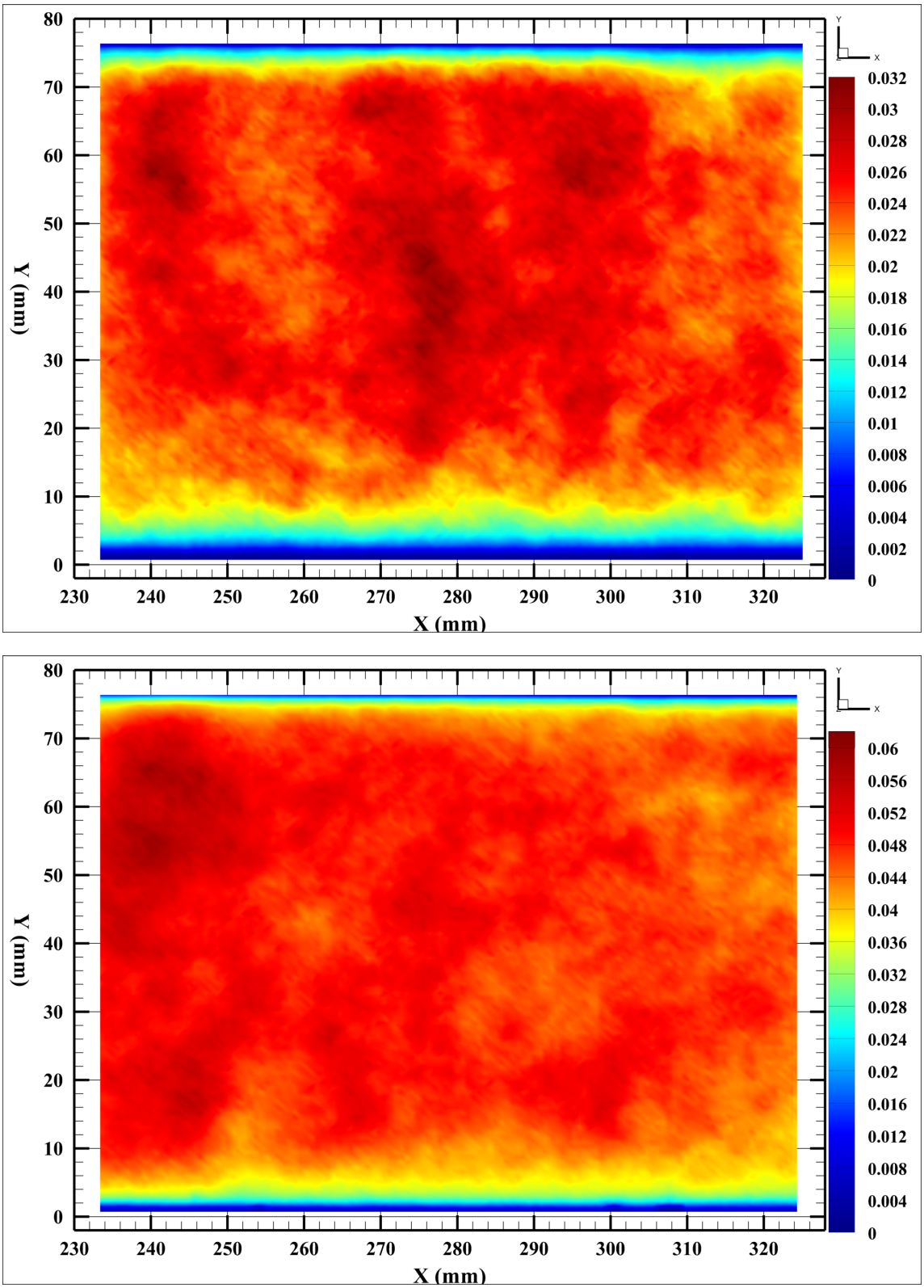

Figure 7.3: Color contour of turbulent kinetic energy magnitude. Top (a): Re = $3,600$, Bottom (b): Re = $6,100$.

7.1.2 Near-Wall Results

The current PIV experimental setup was arranged to acquire the flow fields within the full-height of the test section. The PIV grid point closest to the wall is at approximately 1 wall unit. The PIV grid spacing was 0.73 mm, which allowed flow structures larger than this value to be resolved. Figure 7.4 is a raw PIV image with overlaid instantaneous particle displacement vectors and the corresponding instantaneous velocity vector fields. In addition, close-up views to the near-wall region are provided in Figure 7.4.

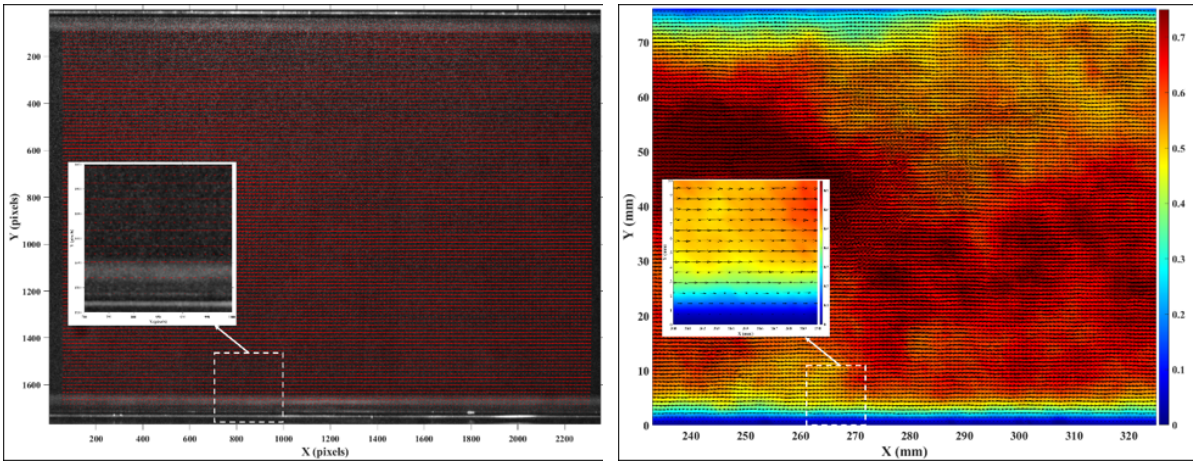

Figure 7.4: Left (a): An instantaneous PIV image with overlaid particle displacement vectors. Right (b): Instantaneous velocity vector fields and color contour of velocity magnitude. Close-up views to the near-wall region are highlighted in the box.

The results of spatiotemporally averaged dimensional profiles of u^+ and u^+_{rms} are presented in Figure 7.5. The dimensionless velocity profile u^+ and the RMS fluctuating velocity profile u^+_{rms} are shown as a function of the non-dimensional wall distance y^+. These dimensionless profiles of u^+ and u^+_{rms} were obtained by spatially averaging the corresponding mean stream-wise velocity and RMS fluctuating stream-wise velocity. The experimental conditions present in the u^+ and u^+_{rms} results were calculated for both particle types and for the two Reynolds numbers. Thus, the results corresponded to polypropylene microspheres (Stk_1) at Re = $4,700$ and Re = $5,900$ and to DEHS

droplets (Stk_2) at Re = $3,500$ and Re = $5,700$.

In Figure 7.5a, following Pope (2001) the universal trend of the turbulent boundary layer was expressed as a linear relation $u^+ = y^+$ in the viscous sublayer ($y^+ < 5$) and a logarithmic slope $u^+ = \frac{1}{k} ln(y^+) + C^+$ in the log-law region ($y^+ > 30$). The u^+ profiles corresponding to all studied Reynolds numbers followed the universal slope of the turbulent boundary layer. However, the obtained dimensional u^+ profiles overestimated the logarithmic slope in the log-law region. As previously found by Huser and Biringen (1993) and Barth et al. (2013), turbulent flows in a square channel could generate higher turbulence in the channel corners compared with turbulent flow over a flat plate, which was used to derive the logarithmic slope. In Figures 7.5a and 7.5b, single-phase DNS results of Huser and Biringen (1993), Lin et al. (2017), and Fornari et al. (2018) are plotted for comparison.

The RMS of fluctuating dimensionless velocity u^+_{rms} as a function of dimensionless wall units y^+ is shown in Figure 7.5b. The magnitude of RMS fluctuating velocity quantifies the degree of fluctuation of the instantaneous flow velocity around the mean flow velocity. An increased u^+_{rms} indicates a higher degree of mixing within the flow. Results from polypropylene microspheres (Stk_1) showed that increasing the Reynolds number resulted in a higher u^+_{rms}, whereas the results obtained for the DEHS droplets (Stk_2) did not show a significant degree of increase in u^+_{rms} with increased Reynolds number. It is possible that the quantitative differences seen in Figure 7.5b could be caused by the flow condition itself since the Reynolds numbers presented are not fully turbulent.

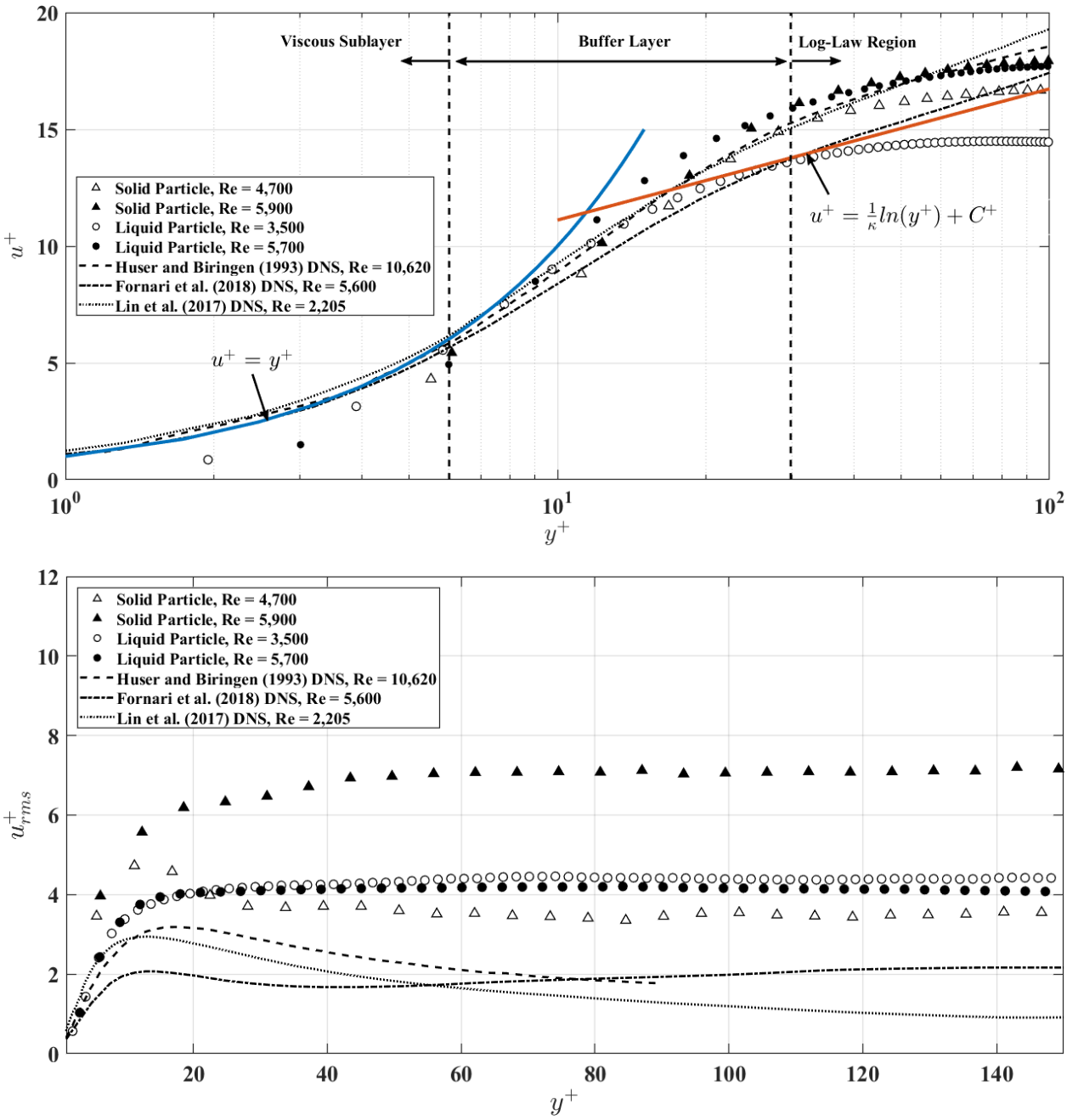

Figure 7.5: Top (a): Spatiotemporally averaged dimensionless velocity u^+ against wall units y^+. Bottom (b): RMS of fluctuating dimensionless velocity u^+_{rms} against wall units y^+. Results are shown for polypropylene particles (Stk_1) and DEHS (Stk_2).

7.1.3 PIV Results Taken at the Inlet of the Test Section

In order to visualize the influence of Reynolds number on entrance effects, PIV data was taken at the inlet of the test section. While the section prior to the test section was meant to allow for flow development, the flow passes through a flanged connection which connects the first section to the second section (test section). The majority of the deposition results are presented for Reynolds number Re $> 3,000$, but for data points collected for $< 3,000$ it can be seen that entrance effects play a small role as the flow passes through the flanged connection which joins the first and second section of the channel. Figure 7.6 illustrates the time-averaged velocity vector field and the normalized velocity magnitude color contour for Reynolds number Re $< 3,000$. From Figure 7.6a and Figure 7.6b, it can be seen that the flanged connection caused a region of increased flow velocity from the test section inlet ($X = 0$ mm) to around $X = 70$ mm for these lower flow velocities. However in Figure 7.6c and Figure 7.6d, the normalized velocity magnitude is shown to approach uniformity indicative of minimized entrance effects most likely caused by the flanged connection. Therefore, the majority of the surface deposition results presented in the following sections are not influenced by this flanged connection and the first section of the channel was successful in its primary role meant for flow development.

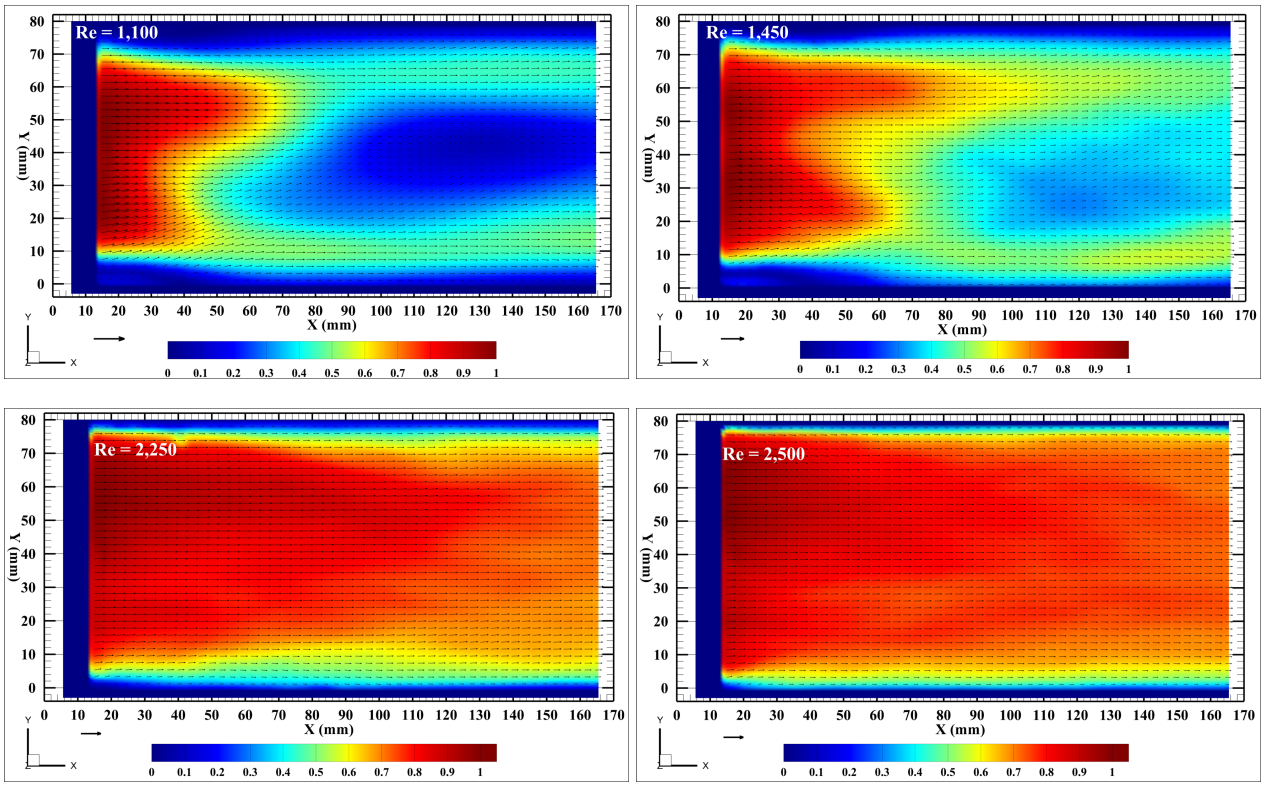

Figure 7.6: Mean velocity vector fields and color contour of normalized velocity magnitude. Taken at channel inlet. Top Left (a): Re = $1,100$, Top Right (b): Re = $1,450$, Bottom Left (c): Re = $2,250$, Bottom Right (d): Re = $2,500$.

7.2 Particle Deposition Results

7.2.1 Particle Deposition Velocity and Particle Relaxation Time

The dimensionless particle deposition velocity u_d^+ is shown as a function of particle relaxation time τ^+. The combined experimental results for polypropylene particles are shown in Figure 7.7a, where u_d^+ is shown for two different surface properties, that is, with or without the addition of a CNT surface coating. The results are also shown for selected cases in which the PIV velocity field was used to measure the friction velocity. Figure 7.7b shows the non-dimensional particle deposition velocity (Equation 5.5) versus the non-dimensional particle relaxation time (Equation 5.15) experimentally obtained for DEHS droplets. For comparison with the model used for empirically estimating the dimensionless deposition velocity, Wood's correlation (Equation 5.11) was plotted for both particle types.

Both results demonstrated that an increase in particle relaxation time reduced the deposition velocity for the experimental conditions of this study. In Figure 7.7, the Reynolds number was found to increase from Re = 700 to Re = $7,000$ which corresponded to a friction velocity of u^* = 0.013 m/s to $u^* = 0.0914$ m/s. The particle deposition velocity in Figure 7.7a ranged from u_d^+ = 0.1583 to $u_d^+ = 0.0129$, whereas the particle deposition velocity in Figure 7.7b ranged from u_d^+ = 0.01303 to $u_d^+ = 0.0032$. For both particle types, increasing the Reynolds number resulted in an increase in τ^+. This makes physical sense because relaxation time, by definition, indicates the time necessary for the particle velocity to equalize with the flow velocity. Increasing the flow velocity (i.e. Reynolds number) for a given particle velocity increases the time necessary for the particle velocity to *relax* to the flow velocity which is again, by definition, an increased particle relaxation time. In this sense, an increased Reynolds number for a given particle diameter followed Wood's model well. Results in which the PIV velocity fields were used to determine the friction velocity were found to closely follow Wood's model. Figures 7.8 and 7.9 show the particle deposition velocity versus particle relaxation time as a log-log scale, similar to the results of many previous studies. In this study, the particle deposition of polypropylene microspheres and DEHS droplets

was governed by the influence of gravitation sedimentation for all flow velocities.

The addition of the CNT surface coating resulted in an increase in the deposition velocity in comparison with an uncoated surface under the same experimental conditions. This result agreed with the results of Gutfinger and Friedlander (1985) and Wells and Chamberlain (1967) who demonstrated an increased deposition rate (i.e. increased deposition velocity) with a fiber-coated surface as compared to a smooth surface and discussed how fibers protruding into the flow offer deposition sites away from the wall, thereby enhancing the deposition process.

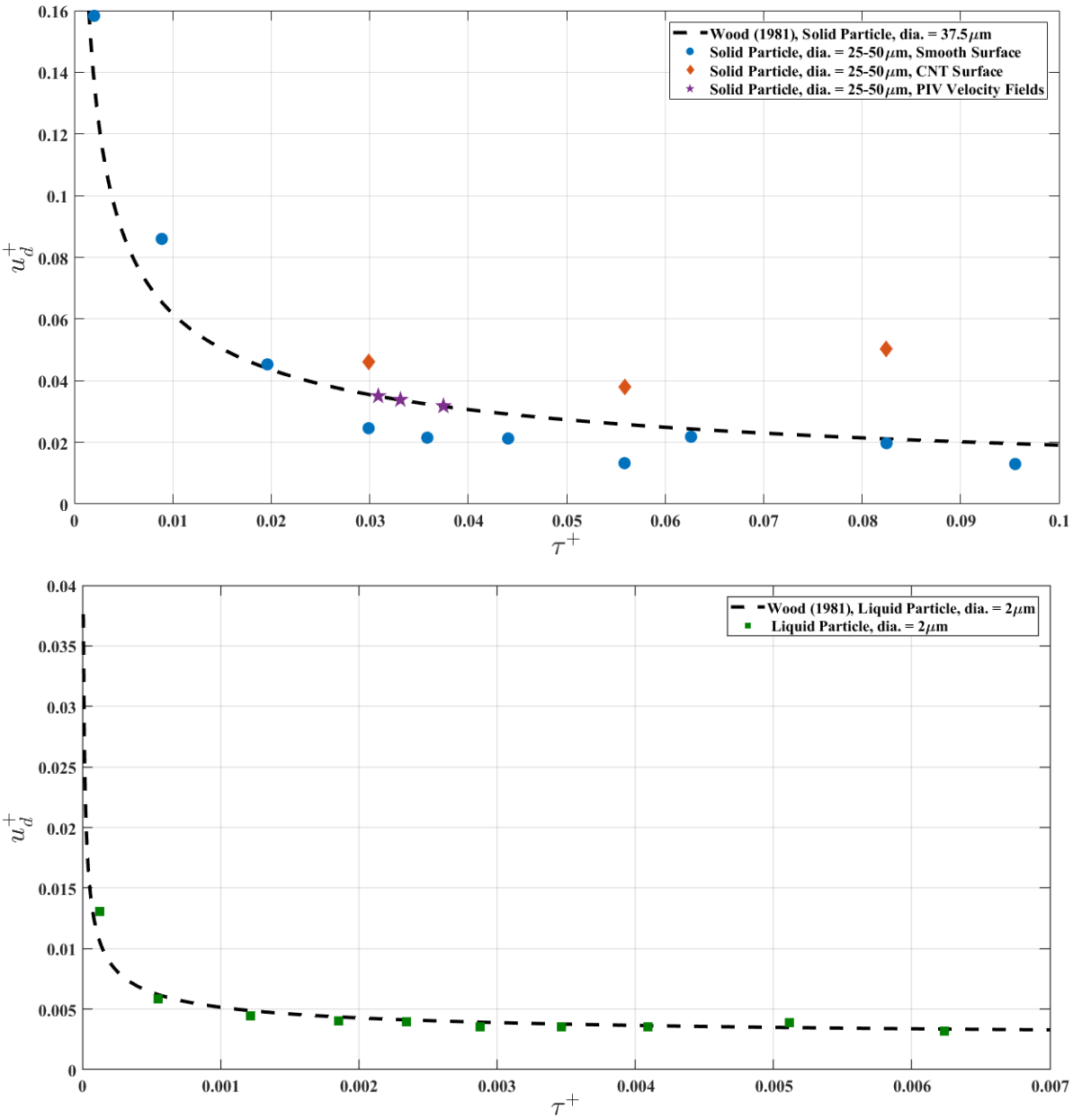

Figure 7.7: Particle deposition velocity as a function of particle relaxation time. Top (a): polypropylene microspheres, Bottom (b): DEHS.

By extending Wood's model as shown in Figure 7.8, a continued increase in particle relaxation time eventually led to an increase in deposition velocity. This was found to be due to the competing terms in Wood's model, in which the magnitude of individual terms reflected the experimental conditions (i.e., increasing Reynolds number for a constant particle diameter). Experimental results conducted with polypropylene microspheres and DEHS droplets were then plotted together and showed the overall comparison with Wood's model. These results also illustrated the regimes in which each term of Wood's model dominated particle deposition. When plotted, the intersection of terms denoted the value of particle relaxation time, in which the deposition to smooth walls due to one term was of the same order as the other term. In Figure 7.8, two intersections are shown, but for clarity, the intersection corresponding to the results with DEHS droplets are annotated with the regimes in which eddy-impaction ($2nd\ Term$) or gravitation sedimentation ($3rd\ Term$) dominated particle deposition (Equation 5.11). The magnitude of the Brownian diffusion term ($1st\ Term$) is very small and a constant, on the order of 10^{-7} and 10^{-9} for the smaller and larger particles, respectively. Therefore, Figure 7.8 only shows the two terms which play larger roles. By decreasing the particle diameter for a given flow velocity, gravitational sedimentation played a larger role in particle deposition since this results in a reduction of relaxation time where the decrease is magnified by square of the particle size.

The shape of Wood's model was determined by the interaction of these three terms. The gravitational sedimentation and eddy-impaction terms determine the left and right limits of Wood's model, respectively. The Brownian diffusion term is constant and thus contributed equally for the flow velocities of a given particle type. For values of τ^+ greater than a critical value τ^+_{crit}, the influence of eddy-impaction on particle deposition causes all curves to converge into one, in which the particle deposition could be described as a power law of the form $u_d^+ = \mathbf{K}\tau^{+2}$, as originally proposed by Owen (1969) and later refined by Wood (1981a). For $\tau^+ \leq \tau^+_{crit}$, Wood's model branches off into separate curves defined by different values of $Sc^{2/3}\tau^{+1/3}$. In this study, $\tau^+_{crit} \approx 10$ for the investigated values of $Sc^{2/3}\tau^{+1/3}$. In comparison to the work of Wood (1981a), the values of $Sc^{2/3}\tau^{+1/3}$ explored in his study resulted in a $\tau^+_{crit} \approx 0.25$. The group $Sc^{2/3}\tau^{+1/3}$ is for a given

particle type (i.e., constant particle diameter and density) and a varying flow velocity. This explains why two curves were created for each particle type at varying flow velocities because each particle type had a different particle diameter and particle density, which resulted in different values of Schmidt number (Sc) and particle relaxation time (τ^+) (Wood, 1981a).

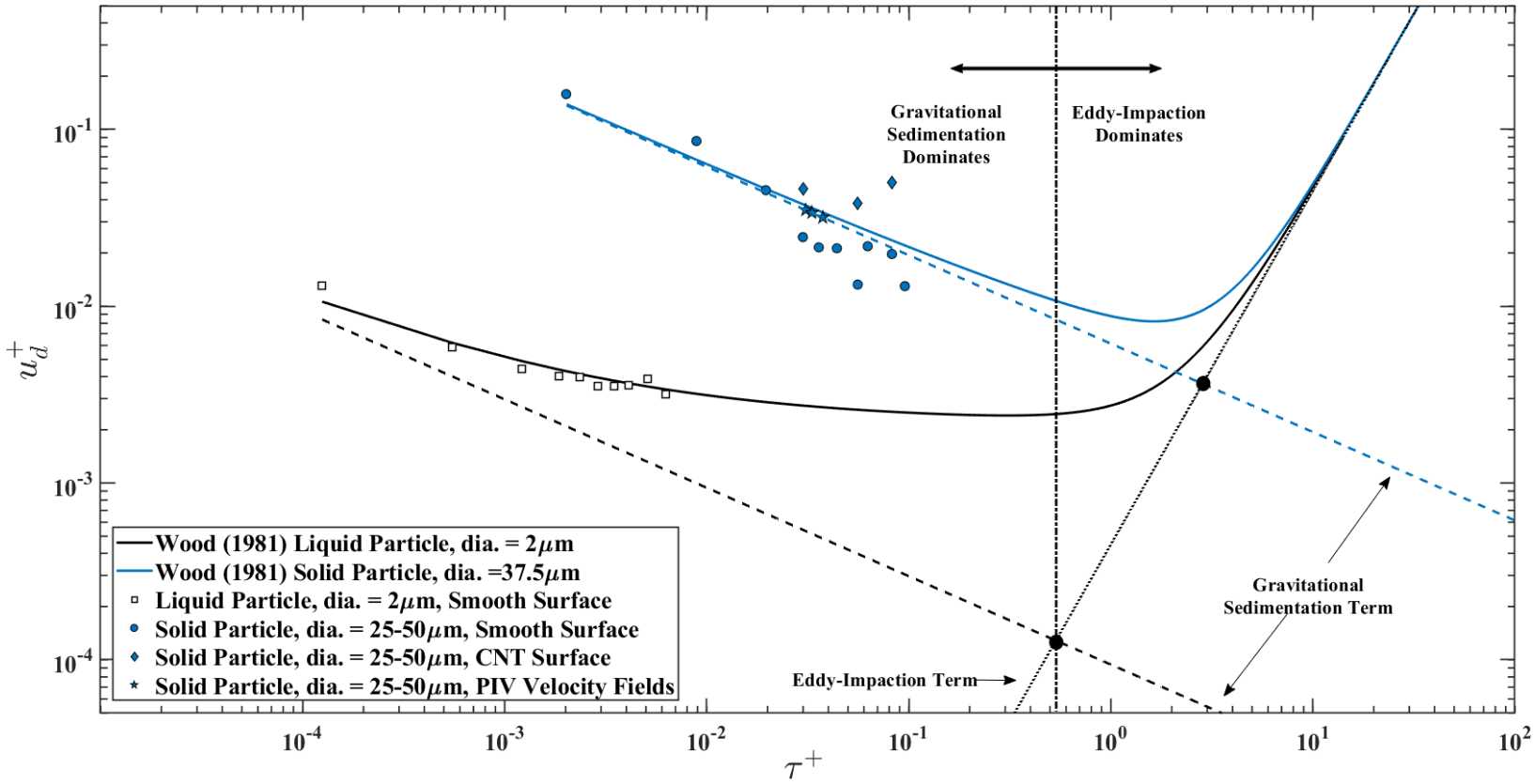

Figure 7.8: Particle deposition velocity as a function of particle relaxation time in the log-log scale. Influence of eddy-impaction (2nd Term) and gravitational sedimentation (3rd Term) on u_d^+ from Wood's Model (1981b).

Figure 7.9 illustrates the comparison with the associated numerical simulation results of this work and with the study of Barth et al. (2013). The associated numerical simulation of this work simulated particle deposition in a square duct, and Barth et al. (2013) experimentally measured the particle deposition in a square duct. The associated numerical simulation results computed the particle deposition velocity by maintaining a constant Reynolds number and increasing the particle diameter, whereas the experimental study computed particle deposition velocity by holding the particle diameter constant and increasing the Reynolds number. Both experimental and numerical studies were compared with Wood's model for these conditions. Likewise, the deposition velocities were compared from both studies for similar values of τ^+.

From the numerical results, in the region where the Stokes number was larger than 10^{-2}, the deposition velocity increased as the relaxation time increased for a constant Reynolds number and varied particle diameter. The numerical results agreed well with Wood's correlation and with the experimental results of Barth et al. (2013). In the experimental study, the average solid particle diameter was used to compute Wood's model ($37.5\mu m$) and the results of experimental to numerical simulation can be compared for similar particle sizes. This can be seen in the from the numerical simulation results for the particle diameters of $30\mu m$ and $40\mu m$ with the same particle density as the polypropylene microspheres. Both experiment and particle simulation show that deposition velocity decreased as normalized relaxation time increased with constant particle diameter. In addition, they have quantitatively similar result in similar particle size at same normalized relaxation time.

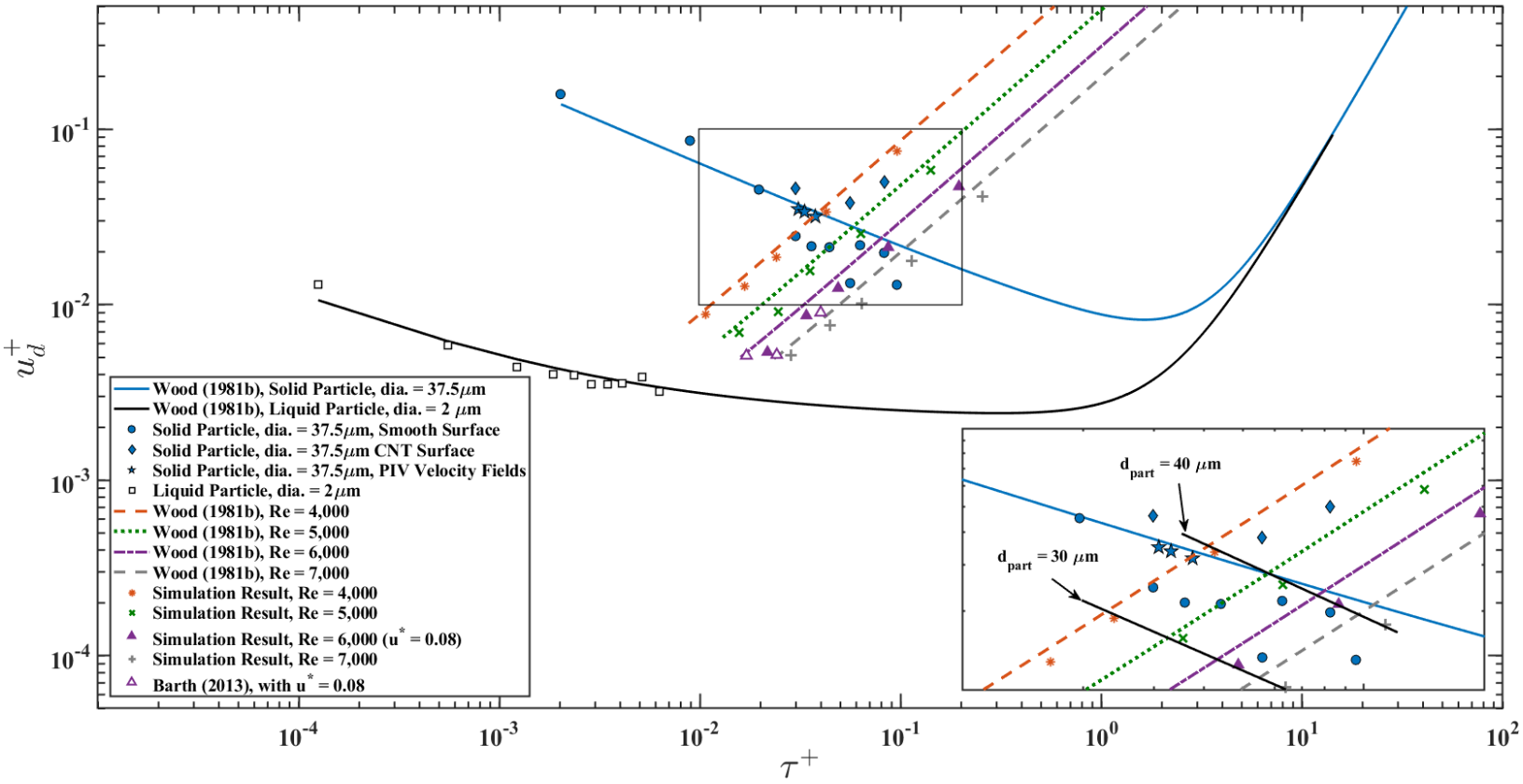

Figure 7.9: Particle deposition velocity as a function of particle relaxation time. Comparison with Wood (1981b), associated numerical results, and experimental results of Barth et al. (2013).

7.2.2 Penetration Efficiency

Effect of Reynolds Number

For a given particle diameter and varying Reynolds number, the general trend observed was that as Reynolds number increased, an increase in particle penetration was observed for both particle types (Figure 7.10). The penetration efficiency was less affected by the increased Reynolds number because it seemed to taper off to an upper limit for the experimental conditions explored. In Figure 7.10, the penetration efficiency of solid particles deposited on a CNT surface coating was tested for only three flow velocities, which corresponded to Re = $3,500$, $5,000$, $6,250$. For each of these flow velocities, the penetration was reduced with the addition of the CNT surface coating, indicating overall enhanced surface deposition. For the range of Reynolds numbers tested, the penetration did not consistently increase with increased Reynolds number but fluctuated to higher or lower levels than the previous Reynolds numbers; however, this fluctuation was attributed to the degree of uncertainty inherent to the calculation of penetration efficiency of either particle type.

Effect of Particle Diameter

For a given Reynolds number and varying particle diameter, an increase in particle diameter resulted in decreased penetration. This can be seen by comparing the liquid aerosol results (smaller diameter) to the solid aerosol results (larger diameter). Increased particle diameter was shown to result in an increased particle deposition velocity. Therefore, the particle deposition velocity was considered to be inversely proportional to the penetration efficiency. This result agrees with the results of McFarland et al. (1991), who found a decreasing trend in penetration efficiency with increasing aerodynamic particle diameters, irrespective of the flow velocity.

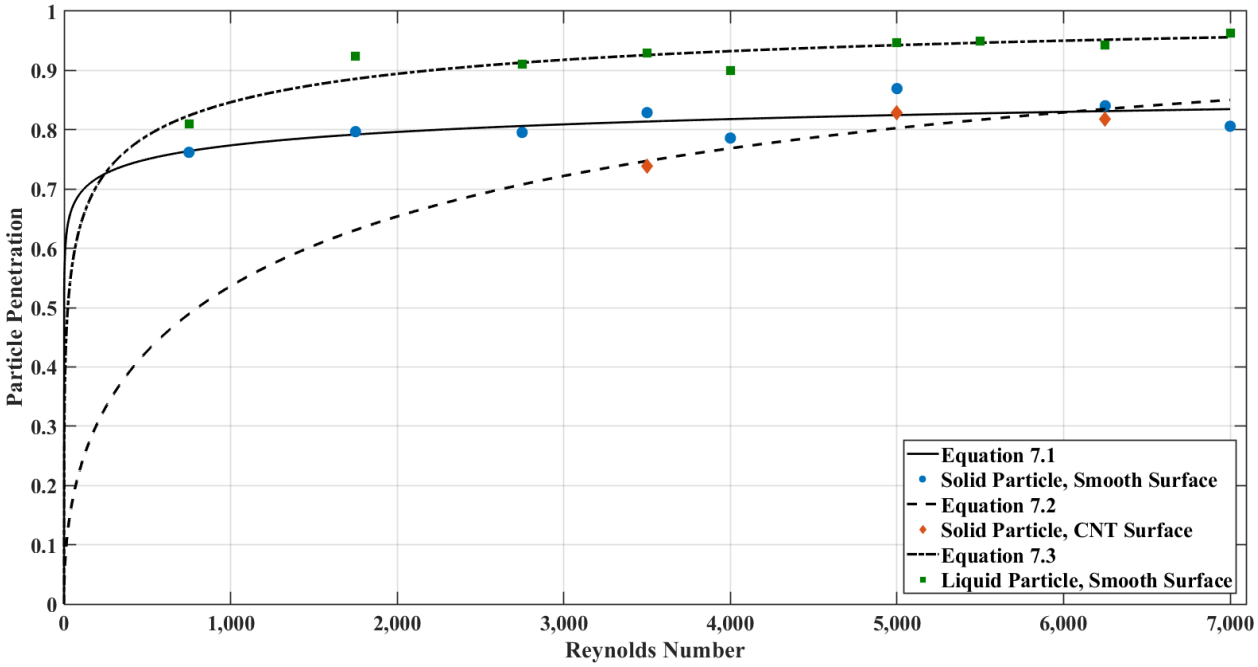

Figure 7.10: Penetration as a function of Reynolds number. Results shown for polypropylene microspheres and DEHS.

Penetration Efficiency Correlation Based on the Experimental Study

We attempted to correlate the penetration efficiency with the flow Reynolds number. The correlation was based on a power law of the form $P = 1 - exp(-\alpha Re^{\beta})$ because the penetration efficiency tapered off to an upper limit with an increase in Reynolds number, where the effect of Reynolds number on penetration was diminished. Likewise, the chosen form of the correlation satisfied the upper and lower limits of penetration. That is, for an infinitely high Reynolds number, no deposition was expected to occur, resulting in $P = 1$. Otherwise, for an infinitely low Reynolds number, all injected particles would instantly be deposited to the surface and would result in $P = 0$. Details of the constants for each curve are found in Table 7.2.

$$P_{Solid,Smooth} = 1 - exp(-0.7512Re^{0.0987}) \tag{7.1}$$

$$P_{Solid,CNT} = 1 - exp(-0.0309Re^{0.4650}) \tag{7.2}$$

$$P_{Liquid} = 1 - exp(-0.3047Re^{0.2629}) \tag{7.3}$$

Table 7.2: Penetration Constants

	$\boldsymbol{\alpha}$	$\boldsymbol{\beta}$	$\mathbf{R}^2$
Eq. 7.1, Solid Particle, Smooth Surface	0.7512	0.0987	0.47
Eq. 7.2, Solid Particle, CNT Surface	0.0309	0.4650	0.79
Eq. 7.3, Liquid Particle, Smooth Surface	0.3047	0.2629	0.83

7.3 Deposition Distribution

Surface deposition scans on the bottom surface of the channel were carried out to characterize the spatial particle deposition concentration. Results presented here are presented for polypropylene microspheres. Each scan required approximately 4 hours to be completed because of the small imaging area. With solid particles, once the solid aerosol was injected, the surface scan began. However, after aerosol injection with DEHS droplets, the deposited droplets tended to deform from their initial circular shapes after impact with amorphous blobs, thus eventually merging with neighboring droplets. This was problematic for the surface deposition measurement technique because the particle cross section was used to calculate the number of particles. Therefore, only the spatial distribution of solid particles is presented.

Measurements of spatial particle deposition concentrations were performed for Reynolds numbers of Re = $3,500$ and Re = $5,000$. Three scans were completed for each Reynolds number, following the scanning grid in Figure 4.6a. In Figure 7.11, the mean of the three scans was computed and used to illustrate the stream-wise and lateral particle deposition concentration. The mean lateral distribution of the five stream-wise locations was computed and is shown in Figure 7.11b. The spatial particle deposition concentration was defined as A_{part}/A_{step} where A_{step} is the area covered by the motorized-traverse in each incremental movement in the scanning direction.

The results of both the stream-wise and lateral scans demonstrate a reduction in the spatial deposition concentration with increased flow velocity. This finding reflects the penetration efficiency trend of the previous section for solid particles (Stk_1). The shape of the stream-wise concentration for Re = $3,500$ was a smooth curve in the flow direction. In contrast, for Re = $5,000$, a nonlinear concentration was observed throughout the test section bottom wall, thus indicating increased turbulence. While the purpose of measuring the spatial deposition concentration along the stream-wise centerline was to mitigate the effect of secondary corner vortices, other forces that were not considered may have played a major role in causing the lumped appearance, as seen for Re = 5,000. As for the trend seen for the lateral distribution, both flow conditions demonstrated an increase near the side wall of the channel. To the best of the author's knowledge, the particle depo-

sition distribution in the lateral direction relative to the stream-wise centerline (Figure 7.11b) was experimentally demonstrated for the first time for deposition enhancement in the corner caused by secondary flow vortices in the corners of a square channel.

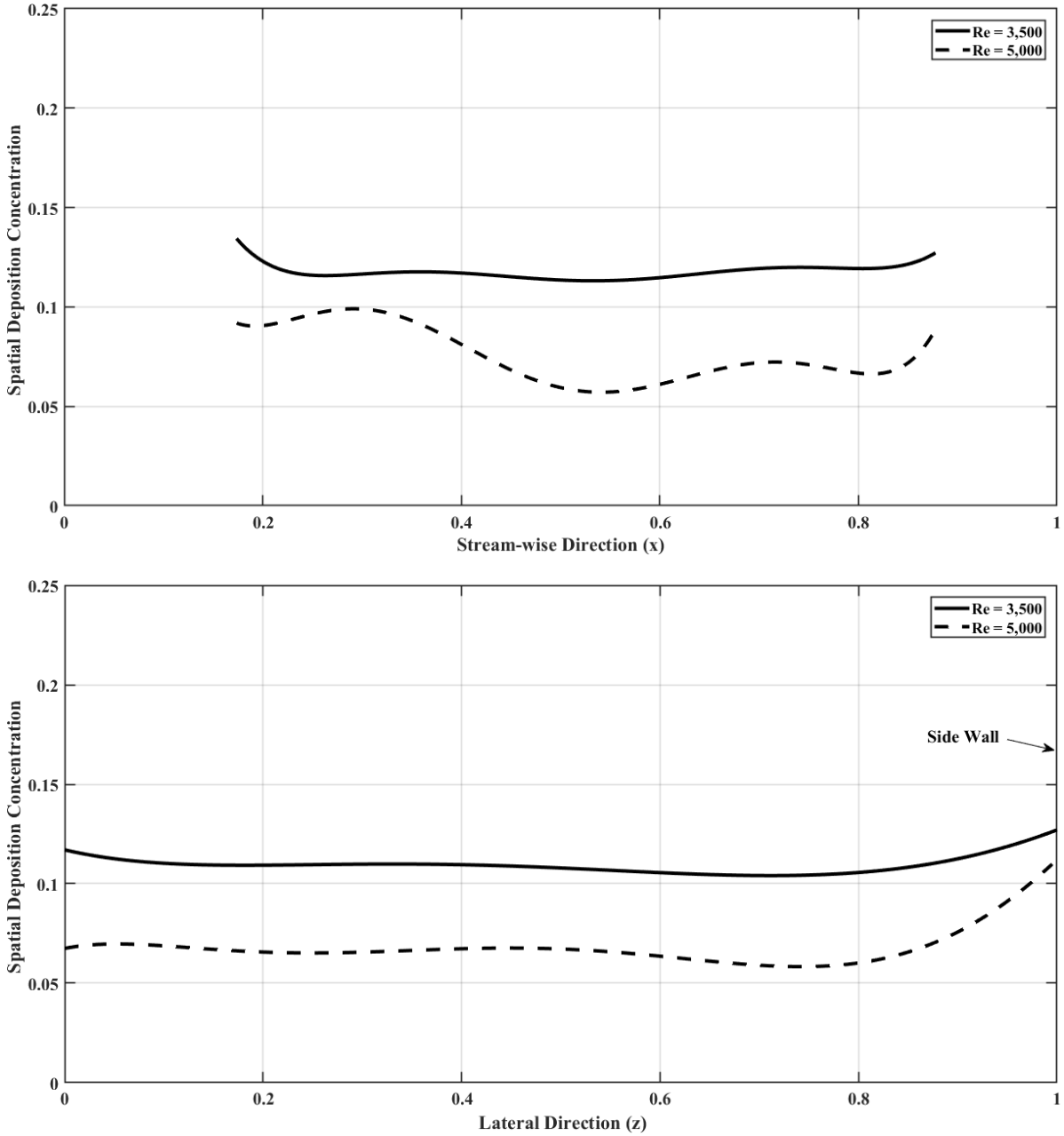

Figure 7.11: Top (a): Particle deposition distribution in the stream-wise direction relative to the inlet of the test section (x=0). Bottom (b): Particle deposition distribution in the lateral direction relative to the stream-wise centerline (z=0). Side wall at z = $\pm$1.

8. SUMMARY AND CONCLUSIONS

In this study, the flow field, free-stream particle concentration, and surface deposition were experimentally measured, and the results were applied to the flow of solid and liquid aerosols in a horizontal square channel. The mean velocity vector field, TKE, and turbulent boundary layer were experimentally measured using PIV. The particle deposition velocity as a function of particle relaxation time was calculated for two particle types with varying flow velocities and compared to a well-known deposition model and to the numerical results. Using a combination of isokinetic probe sampling and a high magnification imaging system, the penetration efficiency and the stream-wise/lateral deposition concentration were measured.

It was demonstrated that the u^+ profiles followed the universal slope of the turbulent boundary layer well but overestimated the logarithmic slope in the log-law region because of the formation of higher turbulence in the channel corners. For both particle types, an increase in particle relaxation time led to a reduction in the deposition velocity for the experimental conditions tested in this study. The increase in Reynolds number for a given particle diameter followed Wood's model well. By comparing the influence of each term in Wood's model, it was found that the particle deposition of polypropylene microspheres and DEHS droplets was governed by the influence of gravitation sedimentation for all flow velocities considered in this study. By decreasing the particle diameter for a given flow velocity, as shown in Figure 7.8, gravitational sedimentation played a larger role in particle deposition since this results in a reduction of relaxation time where the decrease is magnified by square of the particle size. The numerical results agreed well with Wood's correlation, the experimental results obtained by Barth et al. (2013), and with the results of this work. An increased Reynolds number resulted in an increase in particle penetration for both particle types. With the addition of the CNT surface coating, the penetration was reduced, indicating an overall enhanced surface deposition compared to a smooth surface. An increased particle diameter resulted in decreased penetration, which agreed well with the results of McFarland et al. (1991). An equation was proposed which correlated the flow Reynolds number to penetration efficiency

and also satisfied the physical limitation of penetration efficiency. Results of both the stream-wise and lateral scans demonstrate a reduction in spatial deposition concentration with an increased flow velocity. Lastly, deposition enhancement in the corner caused by secondary flow vortices in the corners of a square channel was shown.

REFERENCES

Alexander, L. and Coldren, C. (1951). Droplet transfer from suspending air to duct walls, *Industrial & Engineering Chemistry* **43**(6): 1325–1331.

Aluko, O. and Noll, K. E. (2006). Deposition and suspension of large, airborne particles, *Aerosol Science and Technology* **40**(7): 503–513.

Anand, N. and McFarland, A. (1989). Particle deposition in aerosol sampling lines caused by turbulent diffusion and gravitational settling, *American Industrial Hygiene Association Journal* **50**(6): 307–312.

Asgharian, B. and Anjilvel, S. (1994). Inertial and gravitational deposition of particles in a square cross section bifurcating airway, *Aerosol Science and Technology* **20**(2): 177–193.

Barth, T., Lecrivain, G. and Hampel, U. (2013). Particle deposition study in a horizontal turbulent duct flow using optical microscopy and particle size spectrometry, *Journal of Aerosol Science* **60**: 47–54.

Barth, T., Preuß, J., Müller, G. and Hampel, U. (2014). Single particle resuspension experiments in turbulent channel flows, *Journal of Aerosol Science* **71**: 40–51.

Caporaloni, M., Tampieri, F., Trombetti, F. and Vittori, O. (1975). Transfer of particles in non-isotropic air turbulence, *Journal of the Atmospheric Sciences* **32**(3): 565–568.

Chavez, R., Orea, D., Choi, B.-H., Nguyen, T. D., Vaghetto, R., Anand, N., Hassan, Y. and Sabharwall, P. (2020). An experimental study of solid and liquid aerosol transport in a horizontal square channel, *Aerosol Science and Technology, doi:10.1080/02786826.2020.1786002* .

Choi, B.-H., Orea, D., Nguyen, T., Anand, N., Hassan, Y. and Sabharwall, P. (2019). Numerical study of particle transport and deposition in a horizontal channel using a lagrangian-based mod-

elling approach, *ASME International Mechanical Engineering Congress and Exposition*, Vol. 59438, American Society of Mechanical Engineers, p. V006T06A084.

Dou, Z., Bragg, A. D., Hammond, A. L., Liang, Z., Collins, L. R. and Meng, H. (2018). Effects of reynolds number and stokes number on particle-pair relative velocity in isotropic turbulence: a systematic experimental study, *Journal of Fluid Mechanics* **839**: 271–292.

Eckstein, A. and Vlachos, P. P. (2009). Digital particle image velocimetry (dpiv) robust phase correlation, *Measurement Science and Technology* **20**(5): 055401.

Farmer, R., Griffith, P. and Rohsenow, W. M. (1970). Liquid droplet deposition in two-phase flow, *Journal of Heat Transfer* **92**(4): 587–594.

Fischer, F., Andris, A., Lippmann, W. and Hurtado, A. (2018). Particle deposition by thermophoresis under high-temperature conditions in a helium flow, *Journal of Nuclear Engineering and Radiation Science* **4**(4): 041020.

Fornari, W., Kazerooni, H. T., Hussong, J. and Brandt, L. (2018). Suspensions of finite-size neutrally buoyant spheres in turbulent duct flow, *Journal of Fluid Mechanics* **851**: 148–186.

Friedlander, S. and Johnstone, H. (1957). Deposition of suspended particles from turbulent gas streams, *Industrial & Engineering Chemistry* **49**(7): 1151–1156.

Galletti, B. and Bottart, A. (2004). Large-scale secondary structures in duct flow, *Journal of Fluid Mechanics* **512**: 85–94.

Gavrilakis, S. (1992). Numerical simulation of low-reynolds-number turbulent flow through a straight square duct, *Journal of Fluid Mechanics* **244**: 101–129.

Gelain, T., Alengry, J., Vauquelin, O. and Ricciardi, L. (2019). Tracer dispersion in a duct: Experimental and numerical approach–application to the well-mixing length determination, *Nuclear Engineering and Design* **353**: 110229.

Gutfinger, C. and Friedlander, S. (1985). Enhanced deposition of suspended particles to fibrous surfaces from turbulent gas streams, *Aerosol Science and Technology* **4**(1): 1–10.

Humrickhouse, P. W. (2011). Htgr dust safety issues and needs for research and development, *Technical report*, Idaho National Laboratory (INL).

Huser, A. and Biringen, S. (1993). Direct numerical simulation of turbulent flow in a square duct, *Journal of Fluid Mechanics* **257**: 65–95.

Kaftori, D., Hetsroni, G. and Banerjee, S. (1995). Particle behavior in the turbulent boundary layer. i. motion, deposition, and entrainment, *Physics of Fluids* **7**(5): 1095–1106.

Kine, S. and McClintock, F. (1953). Describing uncertainties in single-sample experiments, *Mechanical Engineering* **75**: 3–8.

Kline, S. J., Reynolds, W. C., Schraub, F. and Runstadler, P. (1967). The structure of turbulent boundary layers, *Journal of Fluid Mechanics* **30**(4): 741–773.

Kvasnak, W. and Ahmadi, G. (1995). Fibrous particle deposition in a turbulent channel flow—an experimental study, *Aerosol Science and Technology* **23**(4): 641–652.

Kvasnak, W., Ahmadi, G., Bayer, R. and Gaynes, M. (1993). Experimental investigation of dust particle deposition in a turbulent channel flow, *Journal of Aerosol Science* **24**(6): 795–815.

Lin, J., Yin, Z., Gan, F. and Yu, M. (2014). Penetration efficiency and distribution of aerosol particles in turbulent pipe flow undergoing coagulation and breakage, *International Journal of Multiphase Flow* **61**: 28–36.

Lin, Z., Yu, Z., Shao, X. and Wang, L.-P. (2017). Effects of finite-size neutrally buoyant particles on the turbulent flows in a square duct, *Physics of Fluids* **29**(10): 103304.

Liu, B. and Illori, T. (1973). Inertial deposition of aerosol particles in turbulent pipe flow, *ASME Symposium on Flow Studies in Air and Water Pollution, Atlanta, Georgia*, pp. 103–113.

Liu, B. Y. and Agarwal, J. K. (1974). Experimental observation of aerosol deposition in turbulent flow, *Journal of Aerosol Science* **5**(2): 145–155.

McFarland, A. R., Wong, F. S., Anand, N. and Ortiz, C. A. (1991). Aerosol penetration through a model transport system: comparison of theory and experiment, *Environmental Science & Technology* **25**(9): 1573–1577.

Montgomery, T. L. and Corn, M. (1970). Aerosol deposition in a pipe with turbulent airflow, *Journal of Aerosol Science* **1**(3): 185–213.

Owen, P. (1969). Pneumatic transport, *Journal of Fluid Mechanics* **39**(2): 407–432.

Phares, D. J. and Sharma, G. (2006). A dns study of aerosol deposition in a turbulent square duct flow, *Aerosol Science and Technology* **40**(11): 1016–1024.

Pope, S. B. (2001). *Turbulent flows*, IOP Publishing.

Raffel, M., Willert, C. E., Scarano, F., Kähler, C. J., Wereley, S. T. and Kompenhans, J. (2018). *Particle image velocimetry: a practical guide*, Springer.

Reeks, M. (1983). The transport of discrete particles in inhomogeneous turbulence, *Journal of Aerosol Science* **14**(6): 729–739.

Sabharwall, P., Skifton, R., Stoots, C., Kim, E. S. and Conder, T. (2013). Piv uncertainty methodologies for cfd code validation at the mir facility, *Technical report*, Idaho National Lab.(INL), Idaho Falls, ID (United States).

Schneider, C. A., Rasband, W. S. and Eliceiri, K. W. (2012). Nih image to imagej: 25 years of image analysis, *Nature Methods* **9**(7): 671.

Sehmel, G. A. (1968). Aerosol deposition from turbulent airstreams in vertical conduits., *Technical report*, Battelle-Northwest, Richland, Wash. Pacific Northwest Lab.

Sharma, G. and Phares, D. J. (2006). Turbulent transport of particles in a straight square duct, *International Journal of Multiphase Flow* **32**(7): 823–837.

Sippola, M. R. and Nazaroff, W. W. (2004). Experiments measuring particle deposition from fully developed turbulent flow in ventilation ducts, *Aerosol Science and Technology* **38**(9): 914–925.

Ström, L. (1972). Transmission efficiency of aerosol sampling lines, *Atmospheric Environment (1967)* **6**(2): 133–142.

Tsuda, A., Henry, F. S. and Butler, J. P. (2011). Particle transport and deposition: basic physics of particle kinetics, *Comprehensive Physiology* **3**(4): 1437–1471.

Wells, A. and Chamberlain, A. (1967). Transport of small particles to vertical surfaces, *British Journal of Applied Physics* **18**(12): 1793.

Westerweel, J. (1994). Efficient detection of spurious vectors in particle image velocimetry data, *Experiments in Fluids* **16**(3-4): 236–247.

Wood, N. (1981a). The mass transfer of particles and acid vapour to cooled surfaces, *Journal of the Institute of Energy* **76**: 76–93.

Wood, N. (1981b). A simple method for the calculation of turbulent deposition to smooth and rough surfaces, *Journal of Aerosol Science* **12**(3): 275–290.

Zhang, T., Yu, S., Peng, W., Sun, Q., Jiang, Y. and Shi, Q. (2017). Resuspension of multilayer graphite dust particles in a high temperature gas-cooled reactor, *Nuclear Engineering and Design* **322**: 497–503.

Zhang, Z., Kleinstreuer, C. and Kim, C. S. (2002). Aerosol deposition efficiencies and upstream release positions for different inhalation modes in an upper bronchial airway model, *Aerosol Science & Technology* **36**(7): 828–844.

APPENDIX A

UNCERTAINTY DETAILS

Kine and McClintock (1953) Propagation of Uncertainty

$$R = f(x, y, z) \tag{A.1}$$

$$U_R = ((\frac{\delta R}{\delta x})^2 + (\frac{\delta R}{\delta y})^2 + (\frac{\delta R}{\delta z})^2)^{1/2} \tag{A.2}$$

Table A.1: Percent Uncertainties for Measured Quantities

Measured Quantity	**Percent Uncertainty**
$\dot{m}_{SPI}$	6.23%
d_{part}	4.44%
$\bar{u}$	0.93%
f	0.009%
$c_{in/out/0}$	15.35%
A_{part}	0.0107%
$t_{injection}$	0.02%

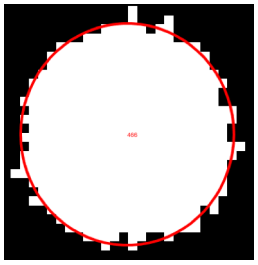

Figure A.1: Error involved in measuring size of particles.

APPENDIX B

PIV ANALYSIS

B.1 Calibration and Pixel-to-Physical Coordinate Conversion

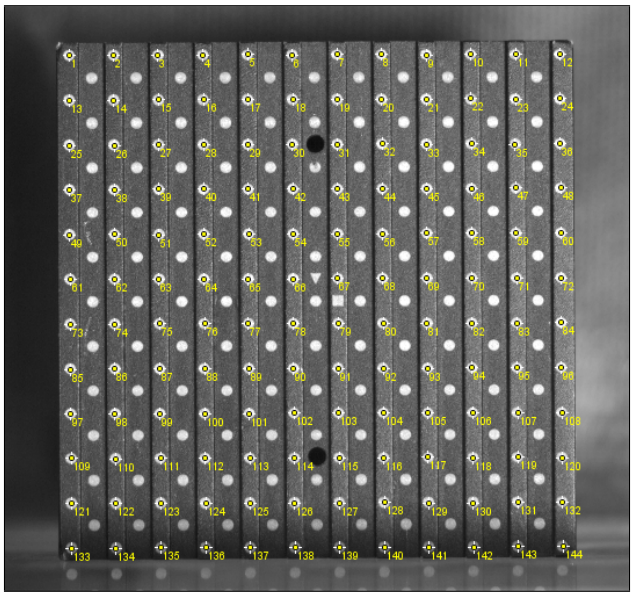

Figure B.1: LaVision calibration target used to find pixel-to-physical scaling ratio. Pixel coordinates of the numbered grid points used to determine δX and δY.

B.2 Overview of In-House PIV Code

Prior to running the PIV code, the raw images were processed to eliminate the background and to isolate the particles in the image.

1. Background calculation

    - The background of the image was found by averaging individual pixel intensities of the raw PIV images.
    - The resulting background image did not have any particles.

2. Background subtraction

    - After calculating the average background from the raw PIV images, the background image was then subtracted from every raw image.
    - The resulting background subtracted image had a background with a pixel intensity of zero whereas the particles did not thereby highlighting the particle motion.

3. Masking

    - Invalid regions were masked prior to running the PIV code. For example, areas of the image which contained the channel walls.

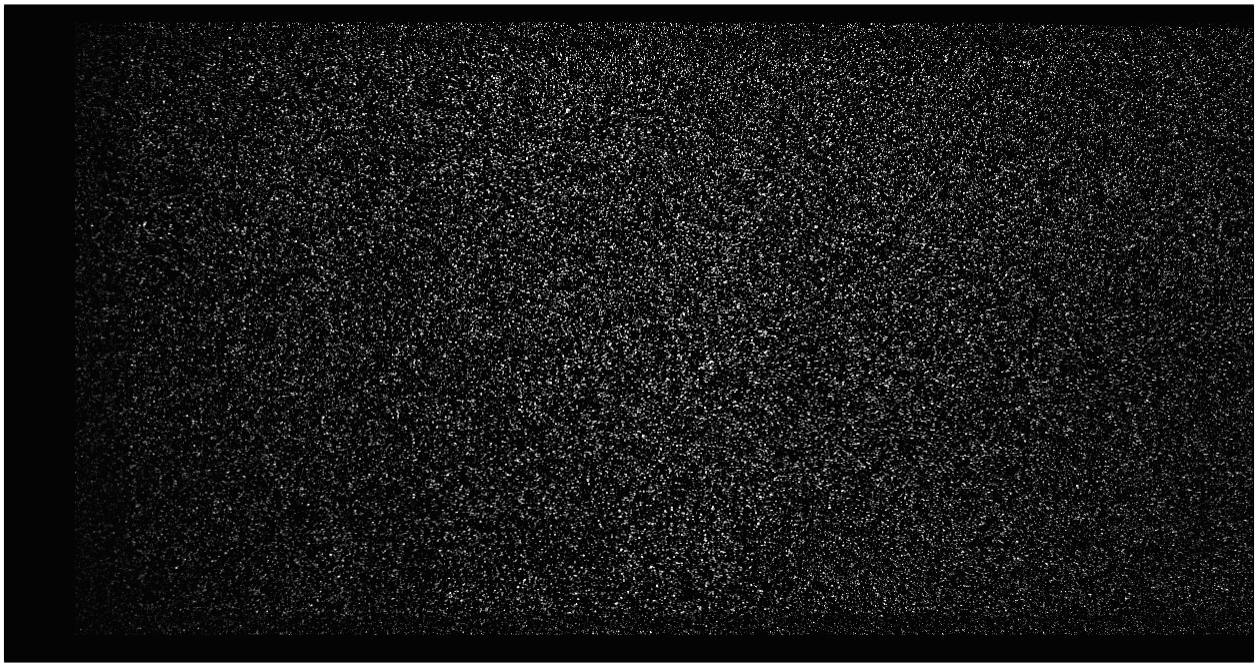

Figure B.2: Background subtracted PIV image.

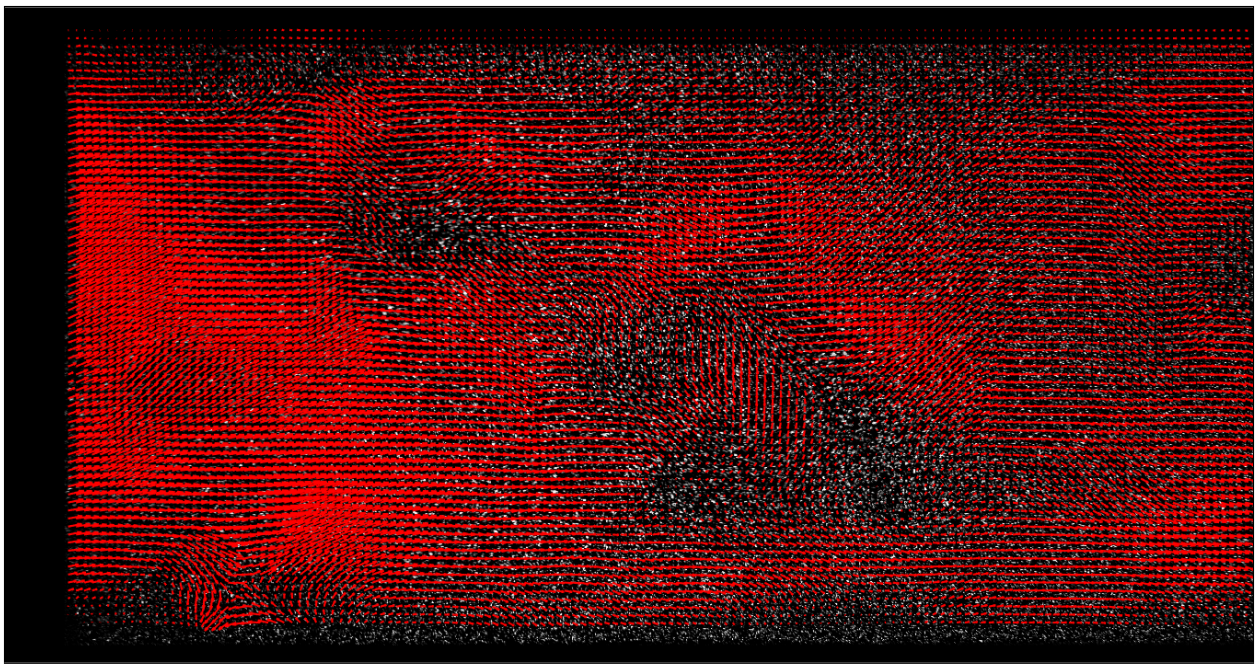

Figure B.3: Instantaneous velocity field overlaid onto background subtracted PIV image.

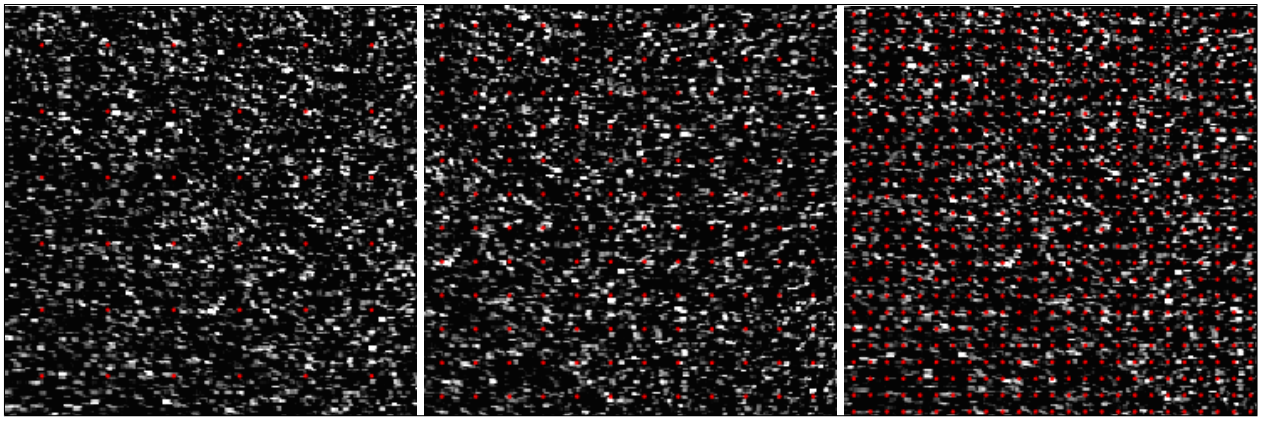

Figure B.4: Multi-pass grid refinement used in PIV code.

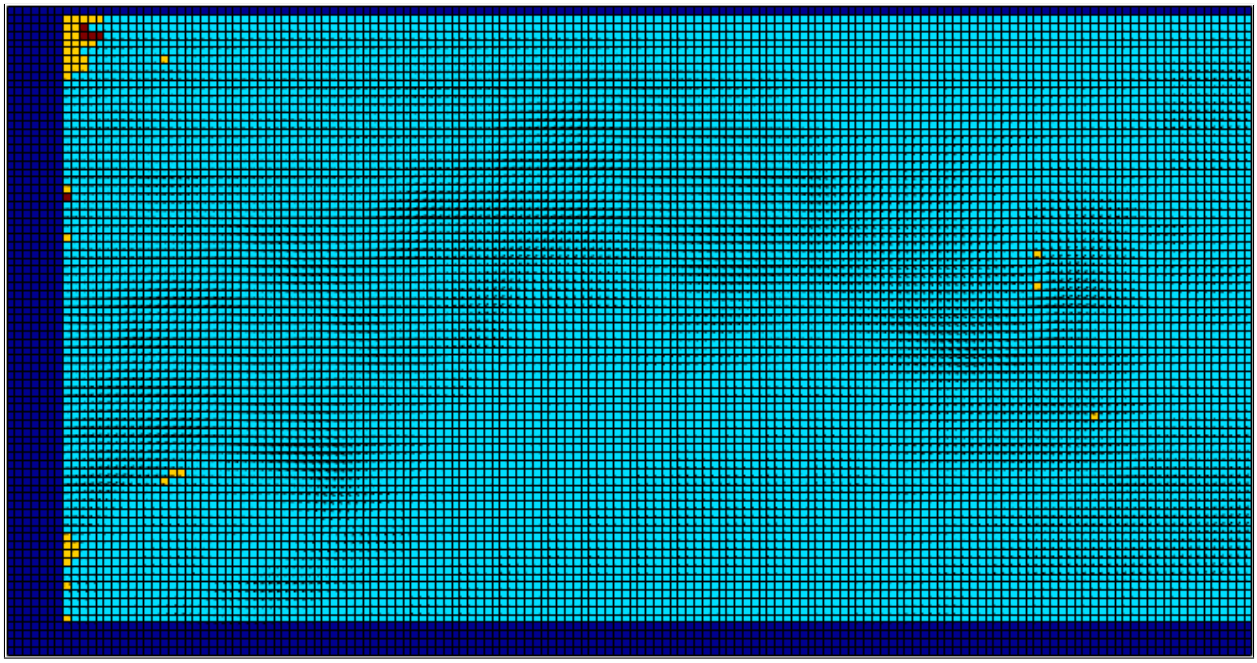

Figure B.5: Evaluation matrix showing grid points where PIV code failed determine the flow direction/magnitude and thereby interpolated by the surrounding grid points. Values shown are results for a single image pair.